The Life Cycle of Thunderstorm Gust Fronts as Viewed with Doppler Radar and Rawinsonde Data

ROGER M. WAKIMOTO

Department of the Geophysical Sciences, University of Chicago, Chicago, IL 60637

Reprinted from MONTHLY WEATHER REVIEW, Vol. 110, No. 8, August 1982
American Meteorological Society
Printed in U. S. A.

Reprinted from MONTHLY WEATHER REVIEW, Vol. 110, No. 8, August 1982
American Meteorological Society
Printed in U. S. A.

The Life Cycle of Thunderstorm Gust Fronts as Viewed with Doppler Radar and Rawinsonde Data

ROGER M. WAKIMOTO

The Life Cycle of Thunderstorm Gust Fronts as Viewed with Doppler Radar and Rawinsonde Data

ROGER M. WAKIMOTO

Department of the Geophysical Sciences, University of Chicago, Chicago, IL 60637

(Manuscript received 5 August 1981, in final form 27 January 1982)

ABSTRACT

This paper presents the time-dependent analysis of the thunderstorm gust front with the use of Project NIMROD data. RHI cross sections of reflectivity and Doppler velocity are constructed to determine the entire vertical structure. The life cycle of the gust front is divided into four stages: 1) the formative stage; 2) the early mature stage; 3) the late mature stage; and 4) the dissipation stage. A new finding is a horizontal roll detected in the reflectivity pattern resulting from airflow that is deflected upward by the ground, while carrying some of the smaller precipitation ahead of the main echo core of the squall line. This feature is called a "precipitation roll". As determined from rawinsonde data, the cold air behind the gust front accounts for the observed surface pressure rise. Calculations confirm that the collision of two fluids produce a nonhydrostatic pressure at the leading edge of the outflow. The equation governing the propagation speed of a density current accurately predicts the movement of the gust front.

1. Introduction

The gust front originating from a mature thunderstorm is a commonly observed phenomenon. The main source of the cold air behind the gust front is the thunderstorm downdraft which is driven by two forces: precipitation drag and evaporative cooling of the raindrops. Once the downdraft reaches the ground, it spreads out and pushes under the warmer, lighter ambient air.

The first thorough investigation of the thunderstorm and its associated phenomenon was by Byers and Braham (1949). They called the outflow the "first gust" and noted that it affected an area much larger than the thunderstorm itself. Fujita (1957, 1963) introduced the term "mesohigh" to describe the pressure rise associated with the evaporative cooling behind the gust front.

With the introduction of the instrumented tower, detailed analyses of the low-level structure of the gust front were undertaken (Colmer, 1971; Charba, 1974; Goff, 1975, 1976; Goff, *et al.*, 1977). Quantitative data on the sequence of meteorological events accompanied by a gust front as it passes a surface recording station were presented. This sequence is:

1) a rise in pressure (pressure rise),
2) a change in the wind direction (wind shift),
3) a sudden increase in the wind speed (wind surge),
4) a drop in the temperature (temperature drop or break),
5) rainfall.

Charba (1974) was the first to present a comprehensive study of the vertical structure of the lowest 500 m of a severe thunderstorm gust front. Soon after, Goff (1975, 1976) recognized that data collected by a tower was a function of the life cycle of the gust front. Thus, he attempted to categorize the stages of the cold air outflow from twenty individual case studies in Oklahoma.

Although these tower analyses presented tremendous amounts of information on the life cycle and structure of the gust front, they were limited by two factors. First, an instrumented tower can only collect data from the lowest 500 m of a gust front. Yet, a typical gust front may extend as high as 2 km above the surface. Second, a tower collects data at a specific location in space. When a time–space conversion is used, a two-dimensional analysis of the gust front can be constructed, but only under the assumption that the gust front is a steady-state phenomenon. The time dependence should be incorporated in the final analysis.

The lack of observations above tower heights has led to the use of the laboratory tank model to deduce the gust front structure (Keulegan, 1958; Middleton, 1966; Simpson, 1969, 1972). Several investigators have recognized that the cold outflow from a thunderstorm might be a type of density current (Simpson, 1969; Simpson, *et al.*, 1977; Charba, 1974). Using this hypothesis the propagation speed of the density current should also predict the movement of the gust front. Unfortunately, these studies have lacked the data to prove unequivocably that the dynamics are the same.

0027-0644/82/081060-23$09.75

As an extension of these past studies, three main objectives of this paper are:

1) to depict the entire vertical structure of the gust front,
2) to obtain the time-dependent analysis of the gust front in order to categorize the different stages of its life cycle,
3) to investigate the dynamics of the gust front. In particular, to investigate the propagation speed of the gust front.

2. Project NIMROD, the data source

Project NIMROD (Northern Illinois Meteorological Research On Downburst) was operated during the spring of 1978. The objective of the research was to study the phenomenon known as a downburst (Fujita, 1978).

A map of the NIMROD network is shown in Fig. 1. There were three Doppler radars forming a triangle outside of Chicago. The locations were O'Hare International Airport (ORD), Yorkville, IL (YKV), and near Monee, IL (CHL). A list of the specifications of the Doppler radars is shown in the Appendix.

Located throughout the network were twenty-seven PAM (Portable Automated Mesonet) stations collecting the air temperature, dew-point temperature, pressure and wind data.

At YKV, 193 rawinsondes were launched in serial ascents, many of them at intervals of thirty minutes. This time resolution was critical in determining the thermal structure through the gust front.

3. Methods of analysis

The case studies analyzed in this paper are gust fronts from squall lines many tens of kilometers in length. The leading edge of such an outflow has often been considered a two-dimensional problem (Fujita, 1957; Charba, 1974; Goff *et al.*, 1977). The winds behind the gust front are generally perpendicular to the frontal interface, so that a radar pointing normal to the front would record Doppler velocities that are very close to the actual horizontal velocity at low elevation angles. Except for one case, the largest elevation angle used in an analysis was no greater than 7°. Thus, the small component of the Doppler velocity contributed by the vertical velocity was neglected, and it is assumed that the Doppler radars were measuring the horizontal motions. RHI cross sections of reflectivity and Doppler velocity were constructed along selected azimuths that were perpendicular to the frontal surface. Whenever possible, the azimuth was modified until a surface PAM station intersected the radial. The information from the PAM station provided the vertical continuity between the surface and Doppler velocity data.

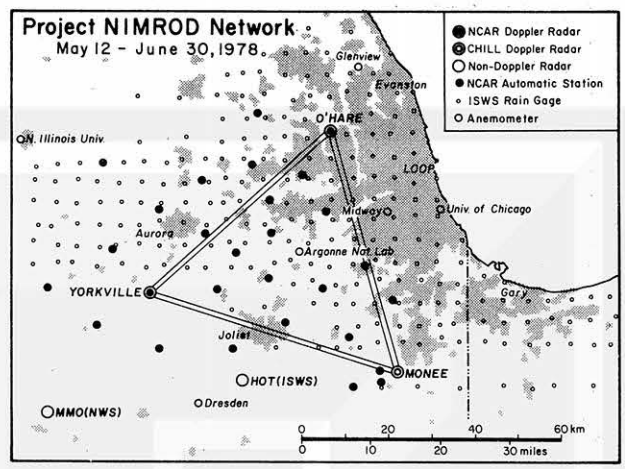

FIG. 1. The NIMROD network.

If the motion of the outflow is two-dimensional, a method to calculate the vertical velocity field is possible using the equation of continuity. There are two aspects of this problem that must be examined: first, if the density variation with height can be ignored; second, whether the flow can actually be considered two-dimensional.

a. Density variation with height

One of the important features of this study is the calculation of the vertical velocity fields from single Doppler radar data. The effect of the density variation with height on the equation of continuity is discussed here.

If there are no local changes of density, the equation of continuity reduces to

$$\frac{\partial}{\partial x}(\rho u) + \frac{\partial}{\partial y}(\rho v) + \frac{\partial}{\partial z}(\rho w) = 0. \qquad (1)$$

If the density variations in the horizontal are considered small and the flow is assumed to be two-dimensional (the latter assumption will be investigated in the next section), Eq. (1) becomes

$$\frac{\partial u}{\partial x} + \frac{\partial w}{\partial z} + \frac{1}{\rho}\frac{\partial \rho}{\partial z} w = 0. \qquad (2)$$

In order to assess the magnitude of the terms, the following scale analysis for the gust front is used:

$$\left.\begin{array}{ll} U \approx 15 \text{ m s}^{-1} & W \approx 5 \text{ m s}^{-1} \approx \tfrac{1}{3}U \\ L \approx 5 \text{ km} & H \approx 2 \text{ km} \approx \tfrac{2}{5}L \\ & \rho = \rho_0 \end{array}\right\}, \qquad (3)$$

where U, W, L and H are characteristic velocity and length scales and ρ_0 is a mean density. Applying these

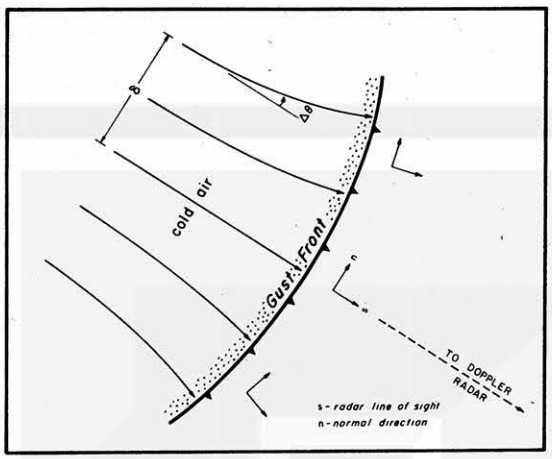

FIG. 2. The coordinate system used for the Doppler radar analysis. The radar beam is perpendicular to the frontal surface along the s-axis. $\Delta\theta$ is the angular deviation from the s-direction in a distance δ taken along the n-direction.

values to Eq. (2),

$$\left.\begin{array}{llll} \dfrac{\partial u}{\partial x} & + \dfrac{\partial w}{\partial z} & + \dfrac{1}{\rho}\dfrac{\partial \rho}{\partial z} w & = 0 \\ \dfrac{U}{L} & \dfrac{5U}{6L} & \dfrac{\Delta\rho}{\rho_0}\dfrac{5}{6}\dfrac{U}{L} & \end{array}\right\} . \tag{4}$$

For most cases, the vertical velocity is not integrated higher than 2 km (~800 mb). Since the temperature differences in the vertical can be considered smaller than the pressure differences,

$$\frac{\Delta\rho}{\rho_0} \approx \frac{\Delta p}{p_0} \approx \frac{1}{5}, \tag{5}$$

where p_0 is a mean pressure. Thus, the scale analysis of Eq. 4 becomes

$$\left.\begin{array}{llll} \dfrac{\partial u}{\partial x} & + \dfrac{\partial w}{\partial z} & + \dfrac{1}{\rho}\dfrac{\partial \rho}{\partial z} w & = 0 \\ \dfrac{U}{L} & \dfrac{5}{6}\dfrac{U}{L} & \dfrac{1}{6}\dfrac{U}{L} & \end{array}\right\} , \tag{6}$$

It is concluded from Eq. (6) that to a good approximation the density variation with height can be ignored.

b. Two-dimensional assumption

The coordinate system used for the Doppler radar analysis is shown in Fig. 2. The horizontal divergence can be calculated using

$$\nabla_h \cdot \mathbf{V} = \frac{\partial u}{\partial x} + \frac{\partial v}{\partial y}, \tag{7a}$$

$$= \frac{\partial V}{\partial s} + V\frac{\partial \theta}{\partial n}, \tag{7b}$$

where Eq. (7b) is in natural coordinates.

The $\partial V/\partial s$ term is the longitudinal divergence which is a measured by the Doppler radar. It attains values on the order of 10^{-2} s^{-1} at the gust front.

If the flow is assumed to be nearly two-dimensional, the second term, called the transversal divergence, should be negligibly small. This term is a measure of the difluence of the wind and can be evaluated by substituting characteristic values obtained from the surface network data. The following is a list of extreme values to assess the largest possible effect of the difluence term (refer to Fig. 2):

$$\left.\begin{array}{l} V = 20 \text{ m s}^{-1} \\ \Delta\theta = 15^\circ \\ \delta = 20 \text{ km} \end{array}\right\} . \tag{8}$$

This leads to a value of

$$V\frac{\partial \theta}{\partial n} = 2.62 \times 10^{-4} \text{ s}^{-1}, \tag{9}$$

for the transversal divergence. This is more than an order of magnitude smaller than the longitudinal divergence at the leading edge of the outflow.

As mentioned previously, this is an *extreme* value of the transverse divergence. If it is assumed to be constant and integrated to the top of the gust front, an estimate of the error in the vertical velocity is obtained. When the height is chosen as 2 km, then

$$W_{\text{error}} = 52.4 \text{ cm s}^{-1}. \tag{10}$$

Apparently, neglecting the transverse divergence will not seriously affect the vertical velocity calculations, and the resultant velocity field will be accurate to ± 0.5 m s^{-1}.

4. The thunderstorm gust front

Even though the term "gust front" is commonly used to describe the low-level outflow from thunderstorms, it has never been clearly defined in the literature. In this paper, gust front is defined as:

> The leading edge of a mesoscale pressure dome followed by a surge of gusty winds on or near the ground. A gust front is often associated with a pressure jump, a temperature drop, and/or heavy precipitation.

Since the case studies to be presented are gust fronts from squall lines, squall line is defined as:

> A narrow band of active thunderstorms (Huschke, 1959).

Using the data from NIMROD, the gust front is depicted as a time-dependent phenomenon. As a result, the life cycle of the gust front is categorized into four different stages. Fig. 3 and Table 1 explain each of the stages. It should be mentioned that these results are based solely on the data from NIMROD.

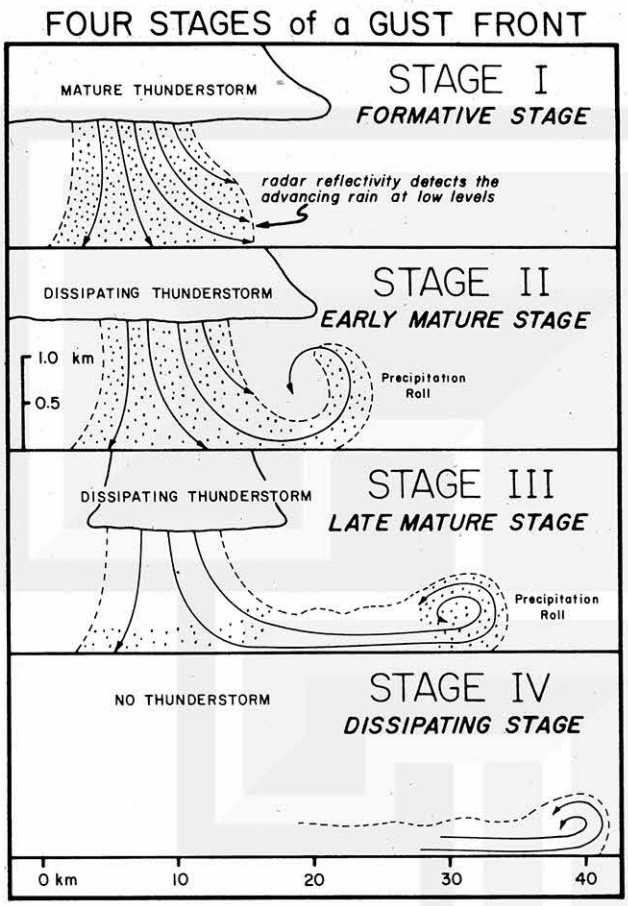

FIG. 3. The four stages of a thunderstorm gust front. The advancing precipitation at low levels is detected by the radar. The "precipitation roll" is a horizontal roll formed by airflow that is deflected upwards by the ground.

It is possible that other evolutionary stages and morphology exist for other storms.

The formative stage of the gust front occurs during the mature stage of the thunderstorm as the leading edge of the outflow propagates away from the main echo core of the squall line. Large reflectivity values are found near the surface as intense rain reaches the ground.

As the thunderstorm begins to dissipate, the gust front enters the early mature stage. At this time, a precipitation roll forms at the low levels. The precipitation roll is a new finding defined as:

> A reflectivity pattern of precipitation shown by the Doppler velocities to be revolving in a horizontal roll at the gust front. The roll is most often observed in stages II and III.

In the late mature stage, the cold air source from the thunderstorm is almost depleted. The gust front becomes a density current as it propagates under the influence of the greater hydrostatic pressure in the cold air.

TABLE 1. Characteristics of the gust front stages.

Stage	Depth	Speed	Radar scattering particles
I Formative	≥1 km	10–20 m s^{-1}	Raindrops from the squall line
II Early mature	1–2 km	10–30 m s^{-1}	Raindrops within a "precipitation roll"
III Late mature	0.5–1 km	10–25 m s^{-1}	Raindrops in the precipitation roll, dust, insects
IV Dissipating	<0.5 km	5–15 m s^{-1}	Dust, insects

The thunderstorm is either on the verge of dissipating, or has completely dissipated by the time the gust front has reached stage IV. The front has propagated far ahead of the rainshaft and is no longer supplied with cold air. The total depth of the gust front becomes smaller as evaporation of precipitation and mixing with the environmental air weakens its structure.

Several analyses from three gust fronts are presented in the next section to illustrate the different stages of the gust front. They are:

Case A: the gust front of 16 June 1978 (stage I)
Case B: the morning gust front of 17 June 1978 (stages II, III, and IV)
Case C: the evening gust front of 17 June 1978 (stages I, II, and III)

The RHI cross sections that were constructed are summarized in Table 2.

a. Stages I–III

By far the best example of the first three stages of the gust front is shown by Case C. The outflow originated from a large squall line northwest of the NIMROD network. Fig. 4 is an isochrone analysis of the wind shift associated with Case C, with the highest recorded mean wind speed after the frontal

TABLE 2. Doppler cross-sections of gust fronts investigated. Times are in CDT.

Stage I	Stage II	Stage III	Stage IV
1009 June 16	0345 June 17	1042 June 16	0400 June 17
1015 June 16	0421 June 17	1045 June 16	0403 June 17
2221 June 17	0427 June 17	0348 June 17	
	0430 June 17	0351 June 17	
	0433 June 17	0357 June 17	
	2224 June 17	2227 June 17	
		2233 June 17	
Total cross-sections 3	6	7	2

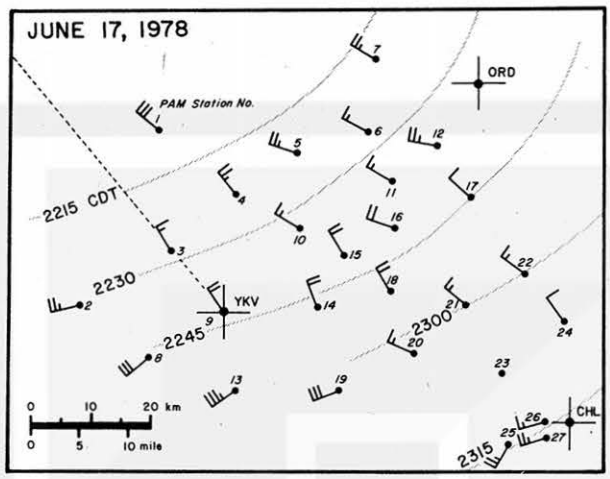

FIG. 4. Isochrone analysis of the wind shift of Case C. The plotted wind vectors are the highest recorded wind speed (1 barb = 10 kt) after frontal passage. The dashed line represents the viewing azimuth from YKV. Stations numbers are indicated near the wind vectors.

passage plotted. A 7°C temperature drop accompanied the gust front as the warm, moist air was replaced by the cool, dry air (Fig. 5).

The PPI radar observations at three elevation angles are presented in Fig. 6. The dashed line represents the 318° azimuth along which the vertical cross sections were constructed. A gust front is clearly visible in the Doppler velocity patterns. A radar thin band (echoes in the form of arcs and bands emanating from thunderstorm squall lines) is evident and its leading edge corresponds with the large gradient of Doppler velocity.

The relationship between thin bands and gust fronts has been well documented, e.g., Brown (1960). It has been suggested that strong refractive-index gradients, insects, birds, or even dust at the leading edge of the outflow are the reasons the gust front is detected by the radar (Batton, 1959). However, in this particular case it will be shown that the thin band is the precipitation roll.

It should be noted that the Doppler velocity is determined from phase shifts rather than an actual power return from the scatterers. As a result, Doppler velocity signatures can be obtained from particles that produce echo returns as low as the minimum detectable reflectivity, even though the reflectivity values may not be recorded to this lower limit on these radar systems due to noise problems. For the YKV, ORD and CHL Doppler radars the minimum detectable reflectivities are 4, 6 and −8 dB(Z) respectively, at a distance of 15 km. These values correspond to the following particle sizes: 54–117μ, 58–126μ and 34–74μ. These size ranges assume that: 1) there is no attenuation, 2) the droplets are spherical and monodispersed, and 3) the concentrations of the droplets range between 1 and 100 cm^{-3}.

Depicted in Figs. 7 and 8 is a complete time history of the development of a gust front. Four times were chosen to construct vertical cross sections: 2221 (stage I), 2224 (stage II), 2227 (stage III), and 2233 (stage III) CDT.

At 2221 CDT (stage I), a rain band is approaching the surface as indicated by the 40 dB(Z) echo core (Fig. 8). Some of this precipitation is flowing horizontally away at a Doppler speed of 22 m s^{-1}. The reflectivity contours for the heights < 1.2 km are slightly ahead from the rest of the squall line, as shown in the model of stage I in Fig. 3. This is a result of the airflow being deflected upwards by the ground while carrying some of the smaller precipitation along with it. Past studies may have overlooked this feature since it occurs on a very small scale. The gust front-relative motion (Fig. 8) depicts strong vertical velocities (10 m s^{-1}) just outside of the 10 dB(Z) isoline in response to the outward push of cold air. The relative motion was calculated by subtracting the propagation speed of the gust front from the horizontal motion field.

Most of the precipitation core has reached the ground by 2224 CDT (stage II), as the 40 dB(Z) echo is much lower and elongated than it appeared at 2221 CDT (Fig. 8). Charba (1974) envisioned the streamline pattern of the formation stage of a gust front to be similar to a vertical jet of fluid striking a plane surface. As shown in Fig. 8, Charba has described an excellent analogy of the flow as there is an upward push of precipitation approximately 20 km from the radar. The flow pattern is well correlated with the reflectivity pattern as the strongest vertical velocities are still confined to the leading

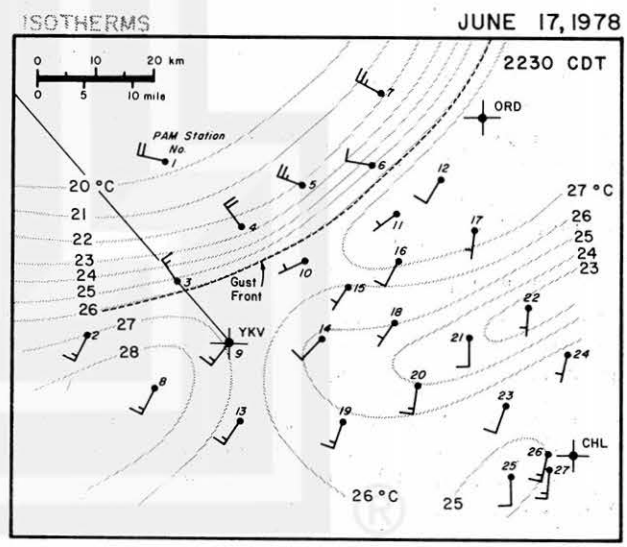

FIG. 5. Isotherm pattern at 2230 CDT for Case C. The leading edge of the gust front is shown by the dashed line. Station numbers are indicated near the wind vectors. Surface wind speeds are in knots (1 barb = 10 kt).

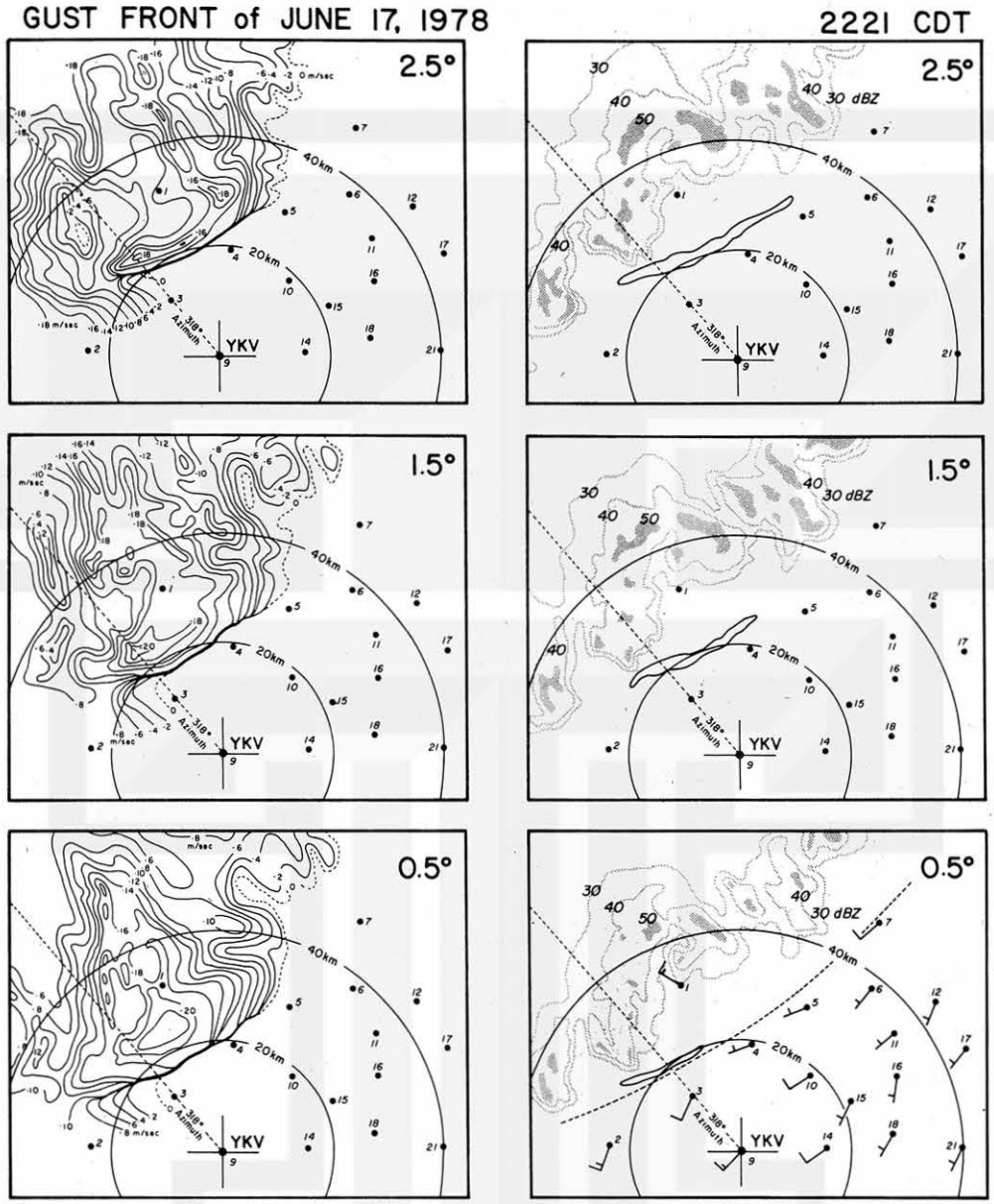

FIG. 6. PPI presentation of Case C from YKV at 2221 CDT. Solid lines are Doppler velocities toward the radar and dashed lines are Doppler velocities away from the radar. Note the radar thin band visible in the reflectivity data. Station numbers are indicated. Surface wind speeds are in knots (1 barb = 10 kt).

edge of the precipitation. This is the beginning of the precipitation roll. In Fig. 8, the maximum echo return within the roll or "head" is 18 dB(Z). If we make the same assumptions on the droplets' characteristics as before, then the size of the droplets would be ~0.1–0.2 mm in diameter. As the precipitation roll passed station 4 (~2225 CDT) the raingauge recorded 0.25 mm of rain in one minute (see Fig. 6).

By 2227 CDT (stage III), the precipitation has pushed well ahead at the low levels, but still appears to have a physical connection with the main downdraft. The 15 dB(Z) isoline located 22 km from the radar is a core of precipitation propagating toward the head of the gust front. It is during stage III that the gust front characteristics are the same as a density current.

The precipitation roll becomes completely disjointed from the main squall line at 2233 CDT (stage III), as shown by the Doppler velocity pattern (Fig. 7). Note how the relative motion vectors conform to the reflectivity pattern in Fig. 8. The relative cir-

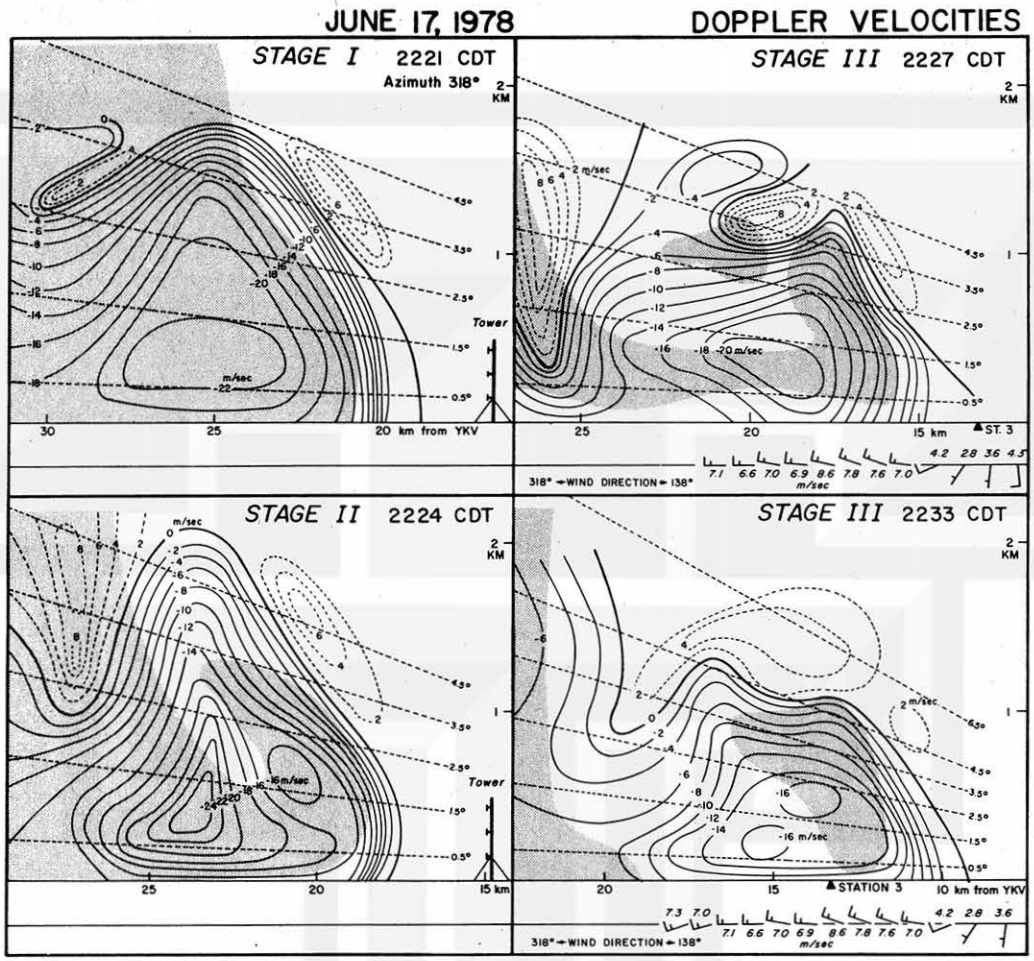

FIG. 7. RHI cross sections of Case C at 2221 (stage I), 2224 (stage II), 2227 (stage III), and 2233 (stage III) CDT. Dashed lines are Doppler velocities away from the radar and solid lines are velocities toward the radar. Gray areas have ≥10 dB(Z) reflectivity (see Fig. 8). Distances are measured from YKV. Surface data are obtained from station 3. Located in the lower right hand corner of the 2221 and 2224 CDT analyses is a 500 m tower.

culation center is very near the center of the 15 dB(Z) isoline located in the head.

A conceptual model of the time history of Case C is shown in Fig. 9. Due to the large time and space variation of Case C, a trajectory analysis was performed. The trajectories were computed by advecting air parcels with the speed and direction of the wind field for each of the four analyses periods. The results of Fig. 10 are similar to the numerical trajectories derived by Mitchell and Hovermale (1977). Included in this figure is the track of the highest echo return within the precipitation roll.

Case C was presented first because it was an excellent example of the first three stages of the gust front evolving in a matter of minutes. Subsequent sections will attempt to examine each individual stage.

b. Stage I—the formative stage

Stage I of the life cycle of a thunderstorm gust front is shown by Case A. Fig. 11 is an isochrone analysis of the wind shift associated with the gust front as it passed through the NIMROD network. The Doppler velocity and reflectivity patterns for four elevation angles at 1009 CDT are presented in Fig. 12. The dashed line represents the 345° azimuth along which the vertical cross sections were constructed.

Figs. 13, 14, and 15 depict the reflectivity superimposed on the Doppler velocities, the ground-relative flow pattern, and the gust front-relative flow pattern at 1009 and 1015 CDT. Both of the times are representative of stage I. In Fig. 15 the gust front at the surface is defined at the stagnation point of the flow.

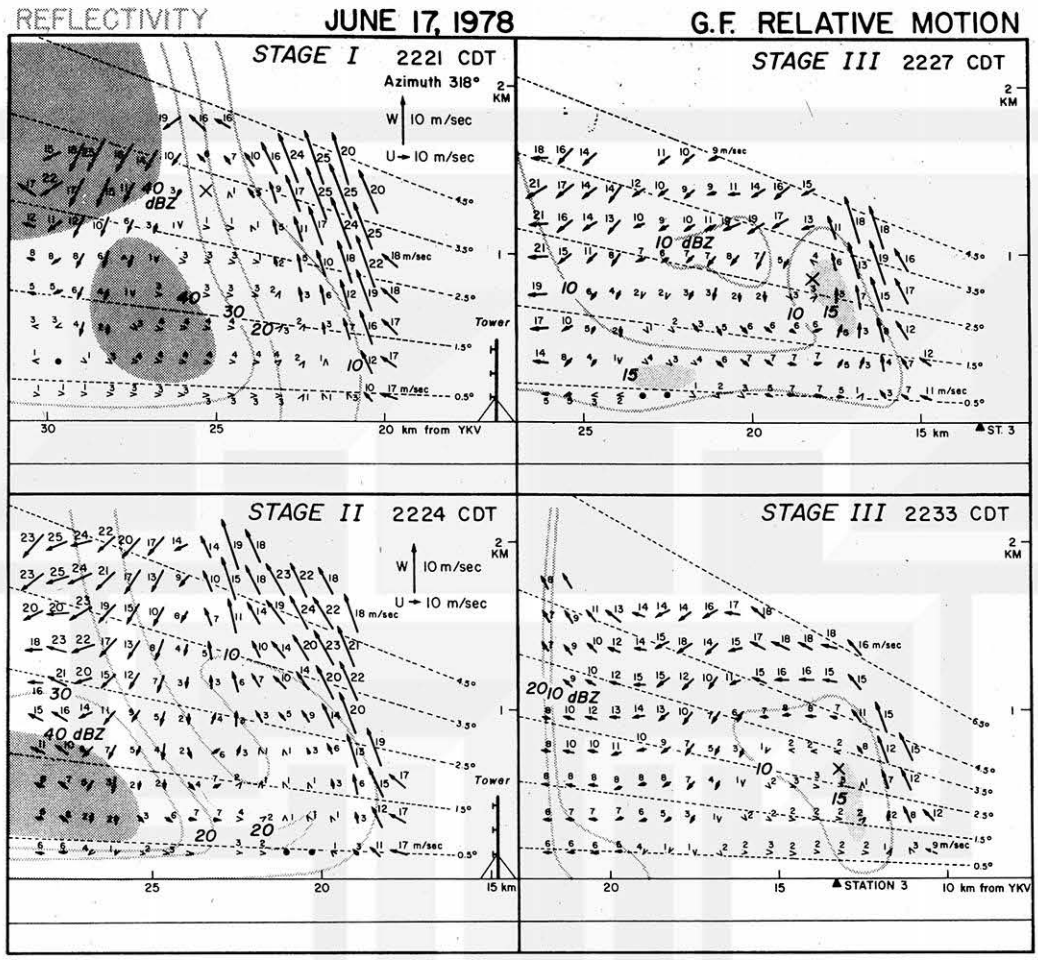

FIG. 8. RHI cross sections of the gust front-relative motion for Case C at 2221 (stage I), 2224 (stage II), 2227 (stage III) and 2233 (stage III) CDT. The cross denotes the relative circulation center. The speeds of the Doppler wind vectors are labeled in the figure. Dark gray areas show reflectivities > 40 dB(Z). Light gray areas show reflectivities > 15 dB(Z) but < 20 dB(Z).

The negative Doppler velocities indicate that the depth of the cold air is approximately two kilometers. In Fig. 13 there are three cores of maximum Doppler velocity that remain a consistent feature from 1009 to 1015 CDT. One of these cores is located over 1 km above the surface. Note the 500 m tower drawn in all of the figures. Such a tower would have been able to sample only one-fourth of the total outflow depth.

There is a very tight velocity gradient at the base of the 60 dB(Z) echo as a result of heavy precipitation which is confirmed by the rainfall measurements in Fig. 16. The largest divergence values at the gust front and at the base of the maximum core of reflectivity is on the order of 10^{-2} s^{-1}. These values led to calculations of +8 m s^{-1} for the forced updrafts at the frontal boundary and −11 m s^{-1} for the maximum downdrafts within the squall line.

There is very good correlation in Figs. 14 and 15 between the surface data obtained from station 4 (anemometer height 4 m) and the Doppler-derived wind vectors. The surface wind speeds are less in magnitude than the Doppler velocities at 0.5° due to the surface frictional effects. As the beam approaches the surface (e.g., ~8 km from YKV at the middle of Fig. 13) the Doppler speeds and surface wind speeds are almost equal.

Examining Fig. 16, it is surprising that there is no change in the surface temperature across the frontal boundary (see Fig. 17). Calculations show that there is a small rise in the wet-bulb potential temperature (θ_w) behind the gust front. This creates a paradox since in the classic model, low values of θ_w are usually brought down from mid-levels behind the outflow.

The only explanation that is plausible are the early morning showers which preceded Case A. Evidently, a surface inversion due to the evaporation was established. The cold air behind the gust front could

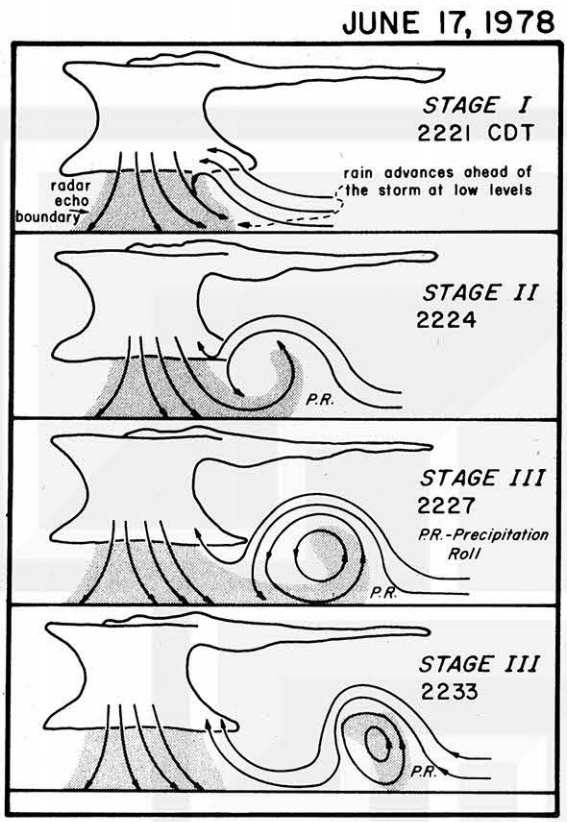

FIG. 9. Conceptual model of the evolution of the gust front of Case C. Note the advancing rain during stage I which leads to the precipitation roll during stages II and III.

not reach the surface-based instrument, but it was detected by a pressure sensor. This is confirmed by the 6 mb pressure rise in Fig. 16. A sounding from Peoria, IL (PIA) in Fig. 23 implies high values of θ_w just above the surface. Mixing by the gust front could have brought these values close to the ground.

This agrees with the results of Greene *et al.* (1977). Their conclusion was that the state of the atmospheric stability in the low levels has a significant effect on surface measurements at the time of a gust front arrival. A low-level inversion can inhibit mixing so that none or only part of the cold air may reach the surface even though the surface wind speeds and the pressure rise indicate the passage of a strong gust front. Several researchers have derived empirical relationships relating expected wind gusts as a function of the observed temperature drop at the surface (Fawbush and Miller, 1954; Simpson, 1969; Hall *et al.*, 1976). Their analyses show that the larger the temperature drop, the more severe the wind gusts. However, it is apparent from observations of this gust front (Case A) that we must re-evaluate the use of surface measurements in determining the severity of a gust front.

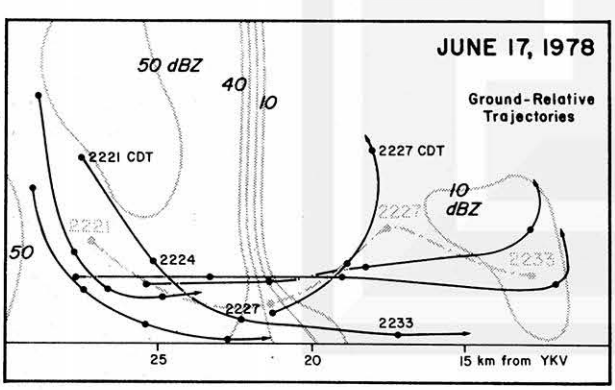

FIG. 10. Trajectory analysis of Case C. The 2233 CDT reflectivity pattern is shown in gray. The gray dash-dot line is the track of the highest dB(Z) echo return within the roll.

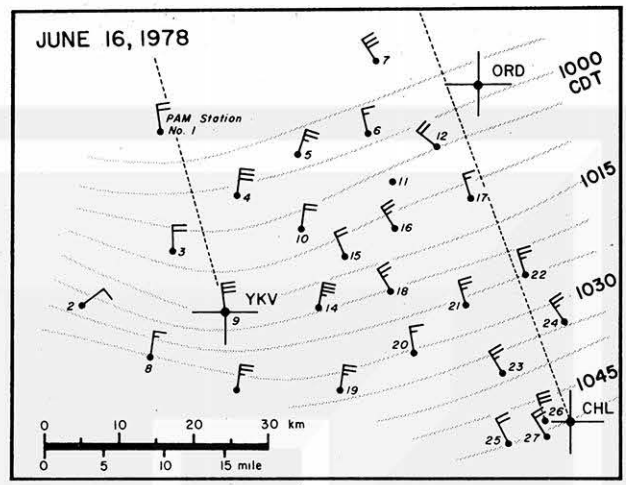

FIG. 11. Isochrone analysis of the wind shift of Case A. The plotted wind vectors are the highest recorded wind speeds after the frontal passage (1 barb = 10 kt). Dashed lines represent the viewing azimuth from two of the Doppler radars along which the RHI vertical cross sections were constructed. Station numbers are indicated near the wind vectors.

c. *Stage II—the early mature stage*

Case B, shown in Figs. 18 and 19, depict stage II of the gust front. RHI cross sections from CHL data are constructed for four times: 0421, 0427, 0430, and 0433 CDT.

Negative Doppler velocities (velocities toward the radar) begin at a point directly under the maximum echo, consistent with the findings of several cases. The core of maximum negative Doppler speeds is located at the leading edge of the squall line. Note the relative circulation center in Fig. 19, as air is being lifted vertically at the gust front and descending behind the circulation center. Motions within the main echo were not plotted because they were very close to being perpendicular to the radar beam at the low levels.

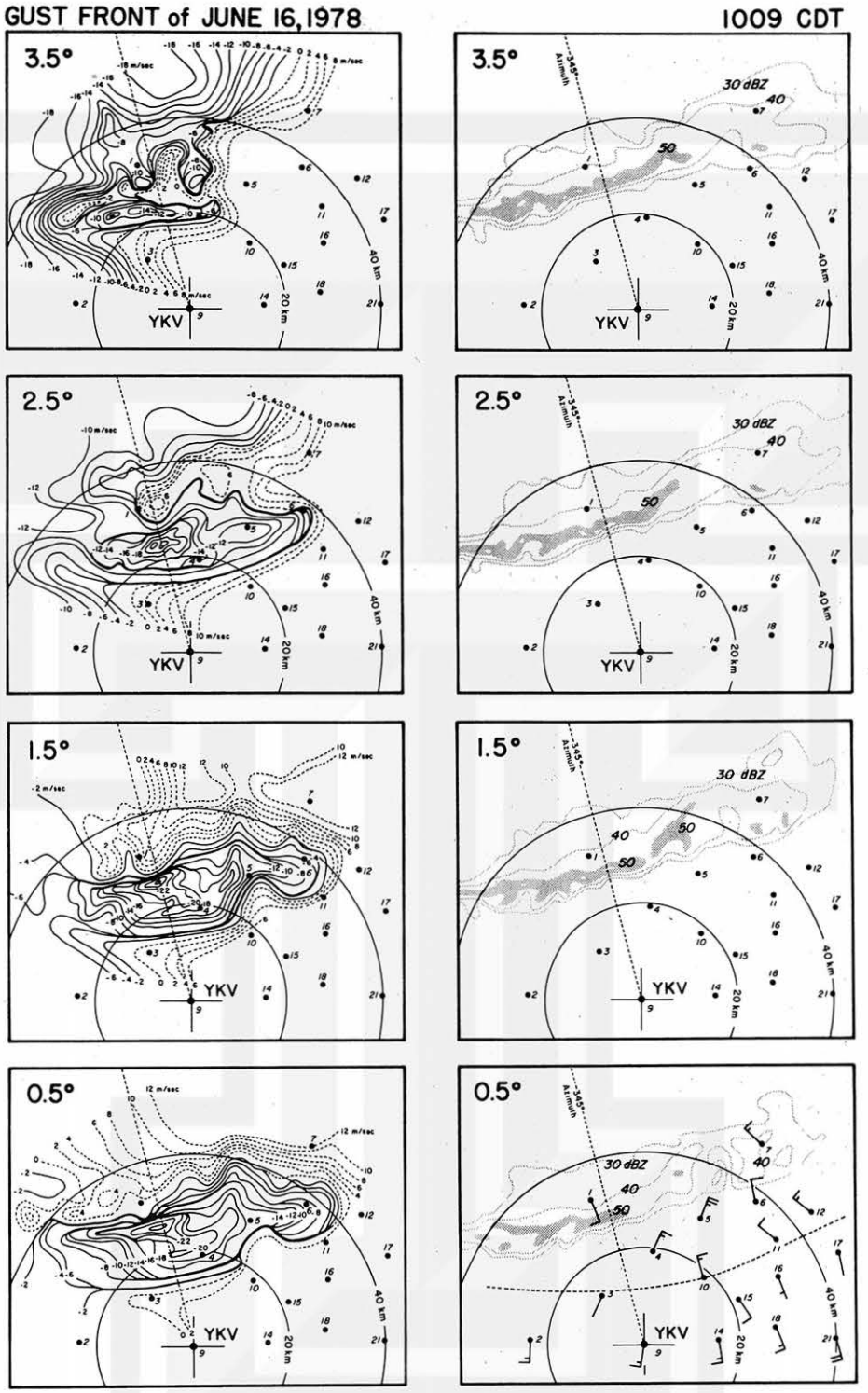

FIG. 12. PPI presentation of Case A from YKV at 1009 CDT. Solid lines are the Doppler velocities toward the radar and dashed lines are the velocities away from the radar. Surface wind speeds (1 barb = 10 kt) are plotted for the lowest elevation angle. Station numbers are indicated.

The 20, 30 and 40 dB(Z) contours for all four analysis times are advected ahead of the other contours at levels below 1 km. As mentioned previously, this is an indication of the airflow being deflected by the ground and being forced horizontally toward the leading edge of the outflow.

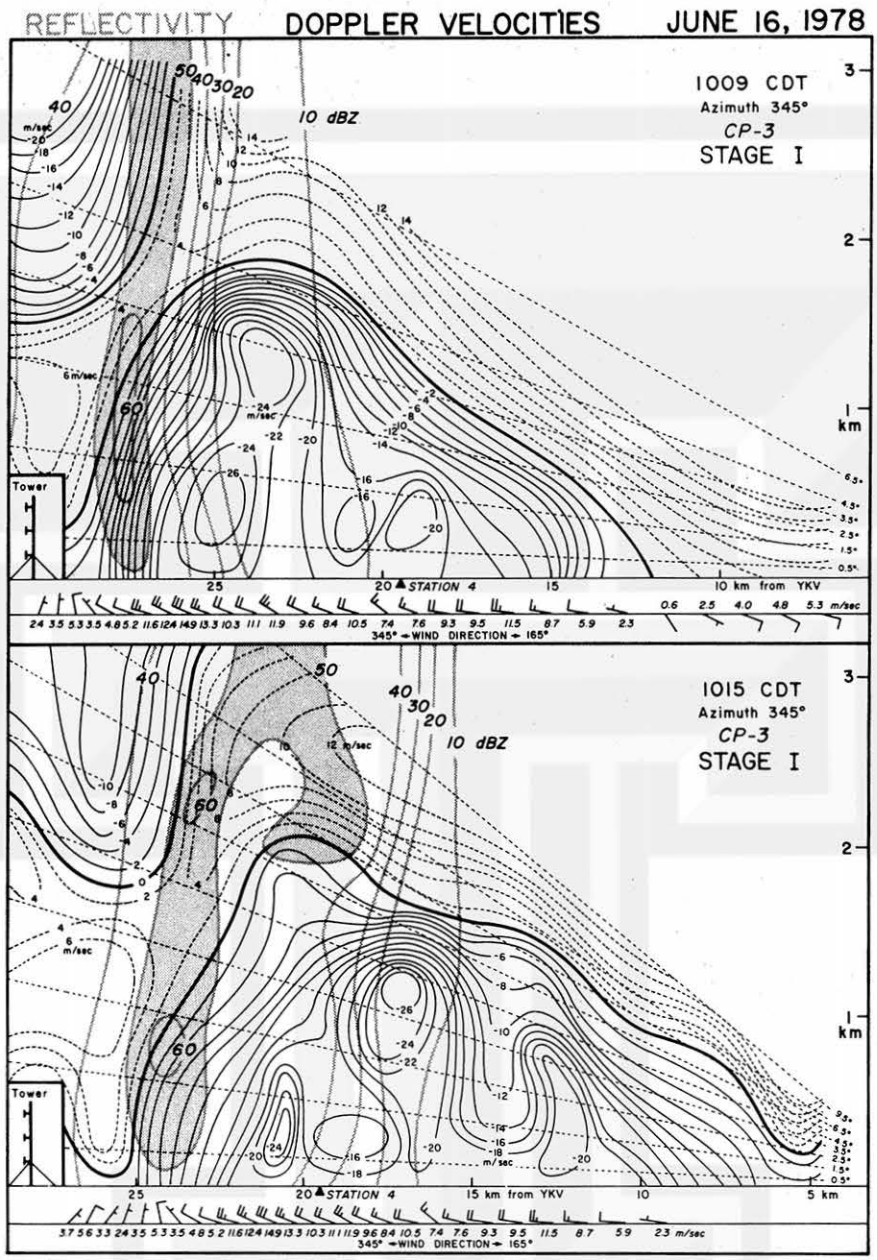

FIG. 13. RHI cross sections of Case A at 1009 and 1015 CDT (stage I). Dashed lines are Doppler velocities away from the radar and solid lines are velocities toward the radar. The gray lines are reflectivity values. The shaded gray are values greater than 50 dB(Z). Propagation speed of the leading edge of the gust front is 20 m s^{-1}. Distances are measured from YKV. Surface data are obtained from station 4.

d. Stage III—the late mature stage

The best example of this stage is presented in Figs. 7 and 8. The description of Case C at 2227 and 2233 CDT, discussed earlier in Section 4a, displays two main characteristics:

1) The precipitation roll is well formed and may become completely disjointed from the squall line.
2) The dynamical characteristics of the outflow are that of a density current, as discussed in Section 5.

e. Stage IV—the dissipation stage

Figs. 20 and 21 illustrate the dissipation stage of the gust front. Three times were analyzed from the YKV radar, 0357 (stage III), 0400 (stage IV), and 0403 (stage IV) CDT. The cold air source had been

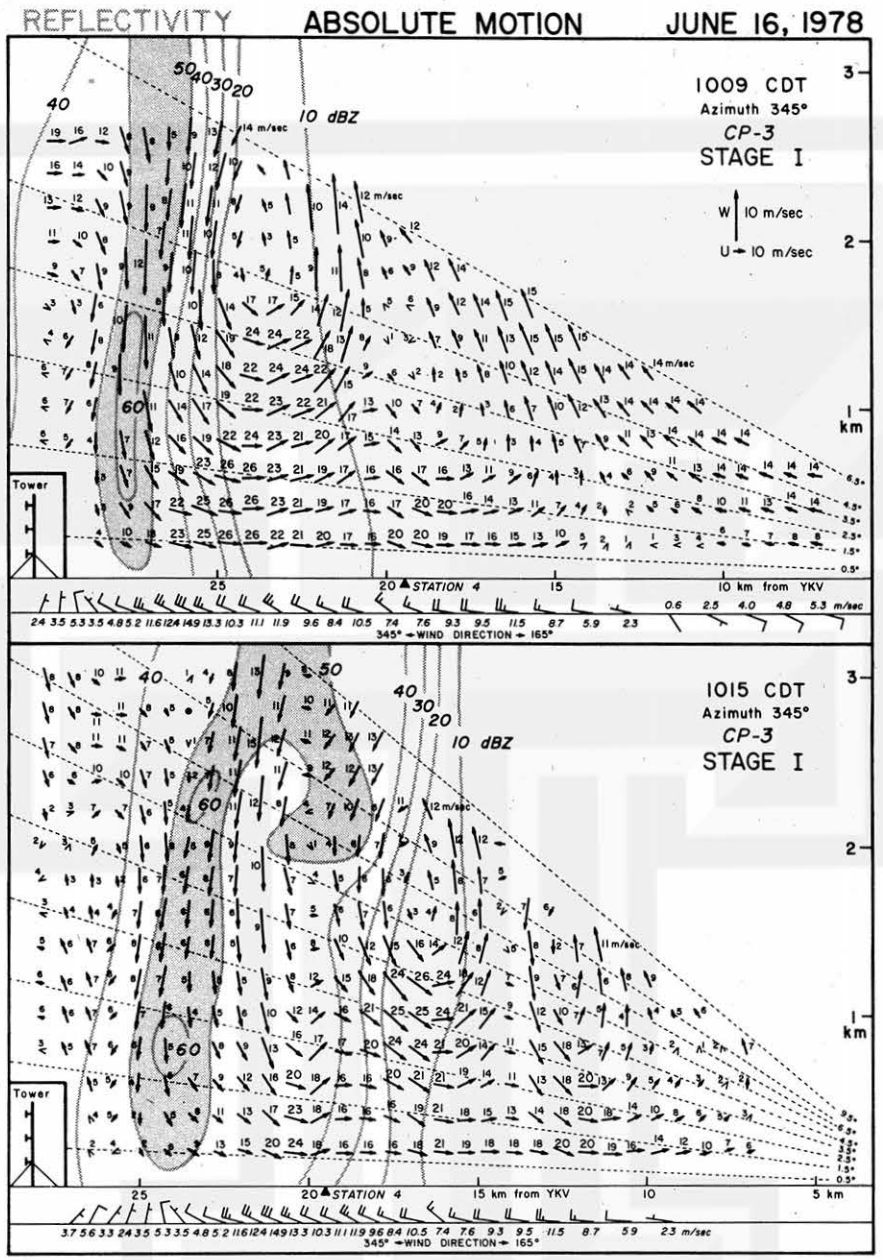

FIG. 14. RHI cross sections of the ground-relative motion of Case A at 1009 and 1015 CDT. Note the strong correlation between Doppler wind vectors (the speeds are labeled in the figure) and surface wind measurements.

depleted because the gust front is 15–20 km ahead of the squall line at 0400 and 0403 CDT. At 0403 CDT the gust front is 5 km from YKV, and within minutes after passing the radar, it completely dissipated and was no longer discernable in the radar or the PAM data.

Three observations in Fig. 20 should be noted:

1) The core of maximum Doppler velocity descends from ~400 m at 0357 CDT to ~100 m at 0403 CDT.

2) The total vertical depth of the negative Doppler velocities decreases with time.

3) The horizontal length of the outflow as determined by the Doppler velocity remains approximately the same from 0357–0403 CDT.

In contrast to the prior analyses, when the Doppler velocities are attributed to very small droplets, it is the author's opinion that entrainment and evaporation have taken their toll on the precipitation by stage IV. During this stage it is probable that dust, insects,

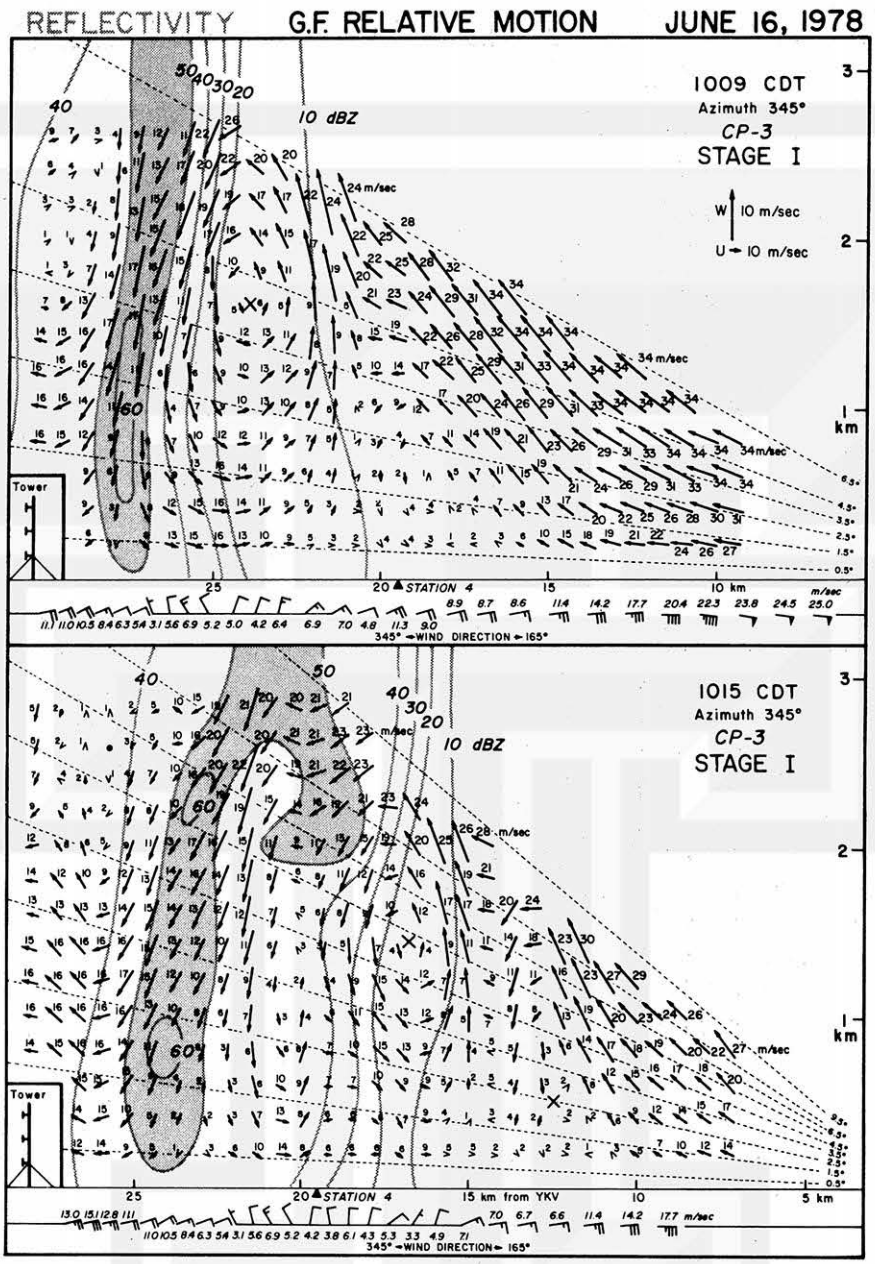

FIG. 15. RHI cross section of the gust front-relative motion for Case A at 1009 and 1015 CDT (stage I). The cross denotes the relative circulation center. The propagation speed of the gust front was 20 m s^{-1}.

or even a thermal discontinuity are the reasons for the Doppler velocities in the clear air.

5. Hydrostatic versus nonhydrostatic pressure

This section combines surface weather observations with serial rawinsonde ascents to determine the nature of the pressure rise associated with the passage of a gust front. Of particular interest is the rise in pressure before the arrival of the cold air. Charba (1974) attributes this rise to a pressure jump caused by a sudden acceleration of a surface cold front. Section 5b discusses another possible mechanism. Also presented is a discussion of a dry layer of cold air observed at the top of the outflow in Case C and a summary of the surface observations during a gust front event.

a. Hydrostatic pressure

The surface observations at station 9 as the gust front of Case A passed YKV are shown in Fig. 22.

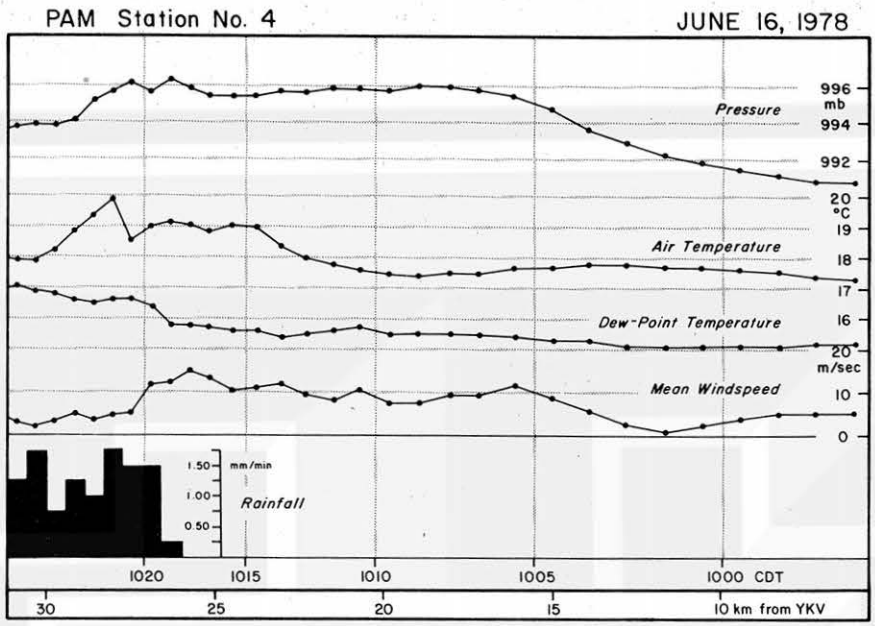

FIG. 16. Surface data from station 4 applicable to the vertical cross section at 1009 CDT. A time–space conversion is used with the propagation speed of the gust front as the advecting speed.

At this time the gust front had evolved to stage III of its life cycle. The soundings taken before and after the gust front passage are shown in Fig. 23. Since there was no launch before the gust front passage, the 0700 CDT (1200 GMT) sounding from PIA, approximately 80 miles to the southwest of YKV was used along with the YKV sounding at 1105 CDT. With the temperature profile from PIA, an estimate of the YKV sounding before the gust front passage was plotted.

The depth of the cold air outflow as seen from the sounding is 3900 m, a much larger value than is normally associated with the gust front. Simpson (1969) was able to show that updrafts and mixing resulting from lifting by the leading edge of the density current decreases to negligible values at a height equal to twice the thickness of the outflow. The 8.2 mb pressure rise is strong evidence supporting a very deep outflow.

Similar analyses of surface and rawinsonde data were performed on Case B (stage IV) and Case C (stage III). These results are presented in Figs. 24, 25, 26, and 27. In Fig. 26, although the rawinsonde appears to be launched late, the high wind speeds behind the gust front advected the balloon through the head (Wakimoto, 1981).

Calculations of the increase in hydrostatic pressure based on the average temperature before and after the passage of the gust front are shown in Table 3. The observed versus calculated values of the hydrostatic pressure rise agree surprisingly well. Errors due to the horizontal drift of the balloon are small since only the data obtained from the lowest few kilometers are used.

b. Nonhydrostatic pressure

A persistent question that appears in much of the literature concerns the rise in pressure before the arrival of the gust front. There have been instances

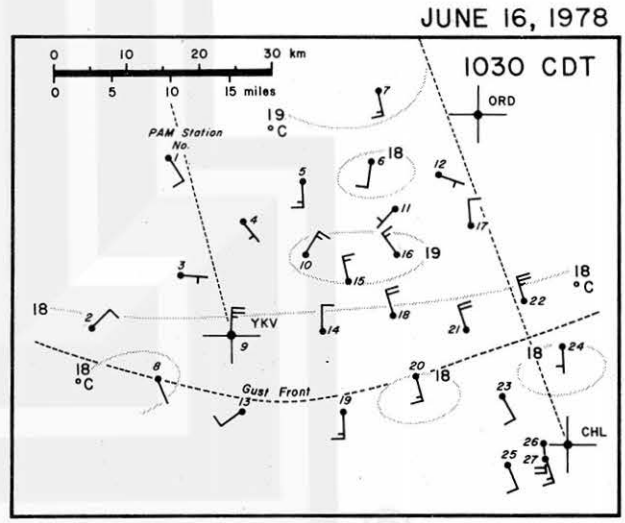

FIG. 17. Isotherm pattern at 1030 CDT for Case A. A surface-based inversion prevented the cold air from reaching the ground (see Greene *et al.*, 1977). Dashed lines from the radars represent the viewing azimuths for the RHI cross sections. Wind speeds are in knots (1 barb = 10 kt). Station numbers are indicated near the wind vectors.

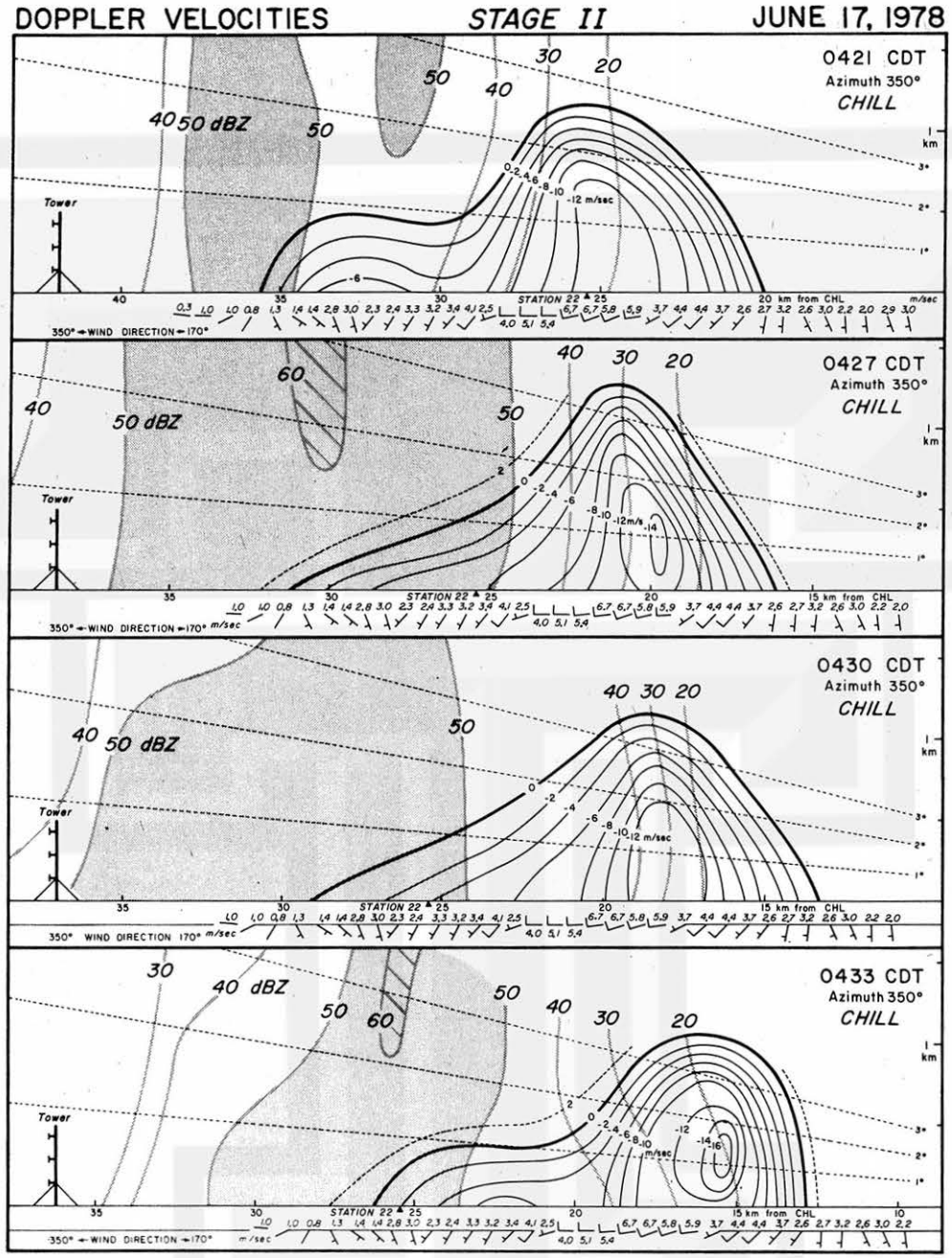

FIG. 18. RHI cross sections of Case B from CHL at 0421, 0427, 0430 and 0433 CDT (all representative of stage II). Dashed lines are Doppler velocities away from the radar and solid lines are velocities toward the radar. The shaded gray areas are reflectivity values greater than 50 dB(Z). Propagation speed of the leading edge is 11 m s^{-1}. Distances are measured from CHL. Surface data are obtained from station 22.

when this pressure rise could be a pressure jump (Tepper, 1950; Fujita, 1963; Charba, 1974), but this phenomenon is not sufficient to explain all of the cases. The nonhydrostatic pressure at the frontal interface appears to be the major contributor to the observed pressure rise. This is apparent when one examines the wind speed trace of Fig. 22. The speeds in both the warm and cold air reach a minimum value at the gust front. To attain such a wind speed profile, a pressure gradient must be generated to decrease the speeds in the warm and cold air.

The theory of the collision of two fluids of different densities generating a pressure is analogous to the pressure nose, which is a sharp rise in pressure due to intense rainfall in thunderstorms (Fujita, 1963).

If the ambient air is stagnant, Newton (1963)

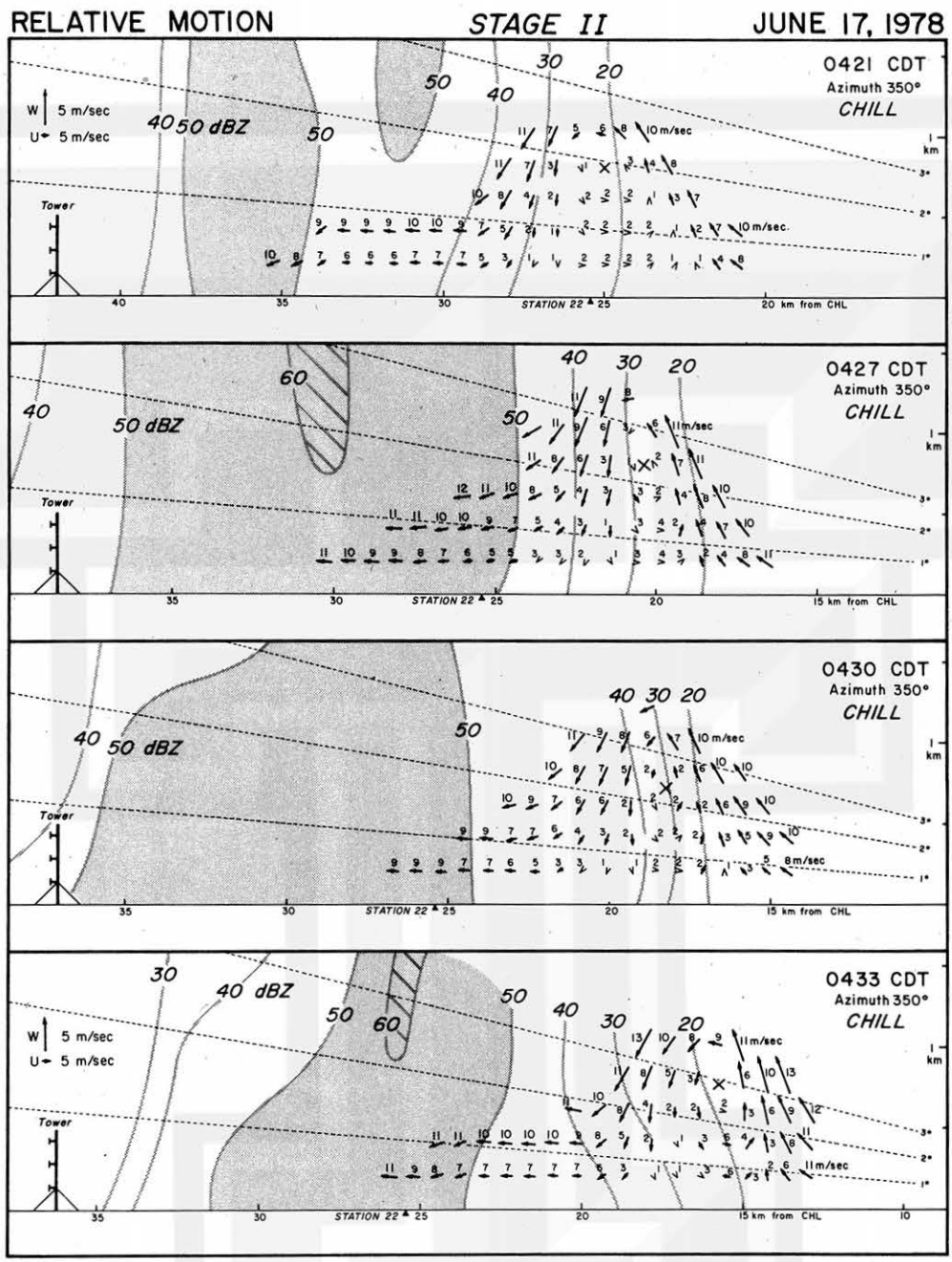

FIG. 19. RHI cross section of the gust front-relative motion for Case B at 0421, 0427, 0430, and 0433 CDT (all representative of stage II). The cross denotes the relative circulation center. The speeds of the Doppler wind vectors are labeled in the figure.

stated that a nonhydrostatic pressure was produced by a cold air outflow. The magnitude would be governed by,

$$P_{nh} = \tfrac{1}{2}\rho V^2, \qquad (11)$$

where P_{nh} = nonhydrostatic pressure, ρ = density of the cold air, V = wind speed in the cold air. This equation can be derived from Bernoulli's equation applied at the stagnation point of a streamline assuming the flow is steady and imcompressible.

Surface observations from station 9 at YKV (Figs. 22, 24 and 26) were used in the calculation of the nonhydrostatic pressure, since the collision of air masses was being measured by a pressure sensor located at the surface.

The nonhydrostatic pressure values in the warm and cold air are summarized in Table 4. Note the

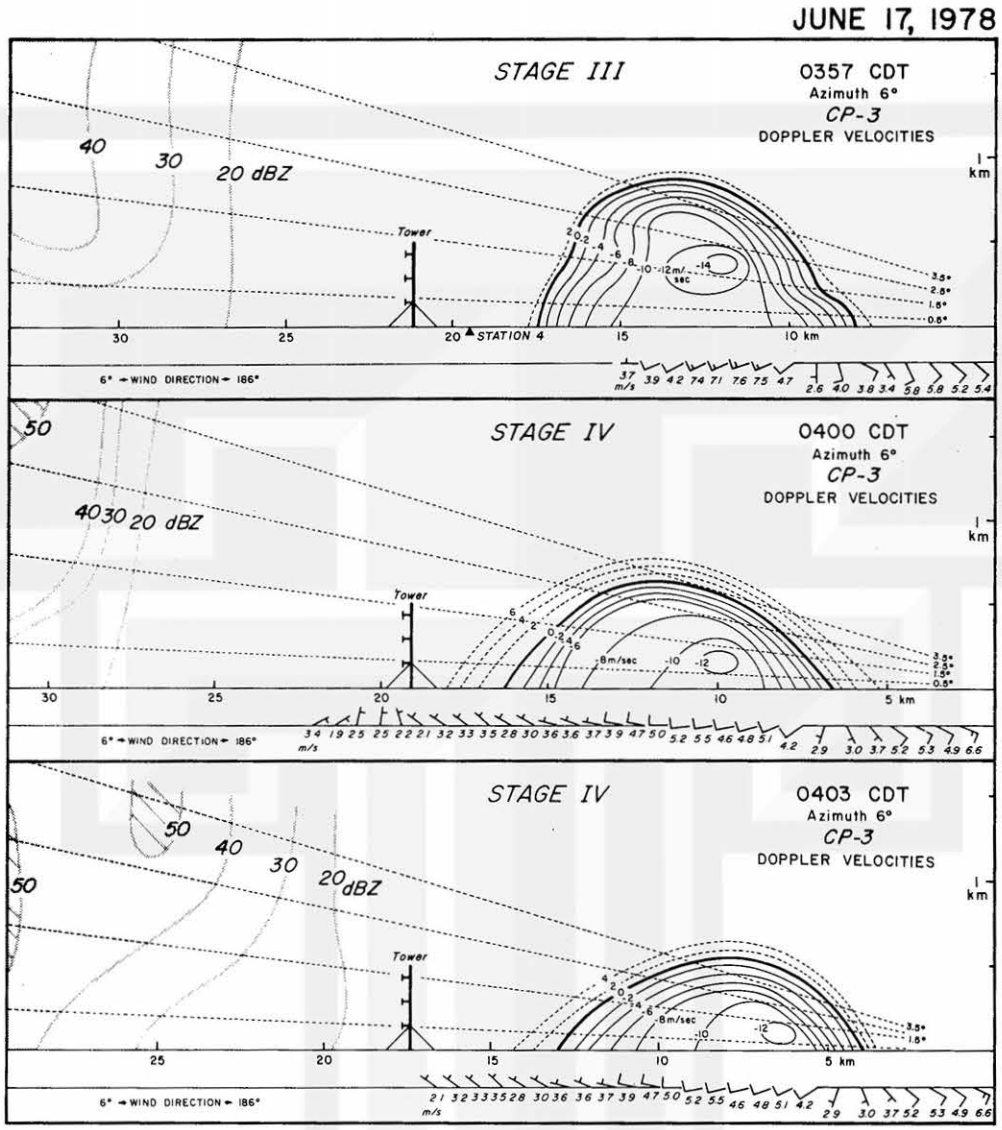

FIG. 20. RHI cross sections of Case B from YKV at 0357 (stage III), 0400 (stage IV), and 0403 (stage IV) CDT. Dashed lines are Doppler velocities away from the radar and solid lines are velocities toward the radar. The shaded gray areas are reflectivity values greater than 40 dB(Z). Propagation speed of the leading edge is 11 m s^{-1}. Distances are measured from YKV. Surface data are obtained from station 4 and station 9.

agreement between the total pressure rise and the observed pressure rise. The surface wind speeds in Table 4 are the components normal to the gust front. There appears little doubt that the pressure rise in advance of the gust fronts observed during NIMROD were caused by the collision of two fluids of different densities.

Case C is similar to the case when the ambient air is stagnant, since the wind direction in the warm air was perpendicular to the propagation of the front.

Re-examining data from Charba (1974), the author arrived at a nonhydrostatic pressure estimate of 3.6 mb across the wind shift. Observations at the surface indicate a pressure rise of 4 mb before the arrival of the gust front. It is possible that the pressure rise that Charba attributes to a pressure jump may, in fact, be due to a collision of air masses.

Another observation in Figs. 22 and 24 is the decrease in the wind speed component normal to the gust front in the warm air to a minimum value just before the arrival of the gust front. This feature has been observed by Goldman and Sloss (1969) and Charba (1974). The minimum appears to correspond with the wind direction shift at the surface. The question arises whether this minimum could be in response to the nonhydrostatic pressure gradient generated by the gust front.

To examine this effect on the environmental winds,

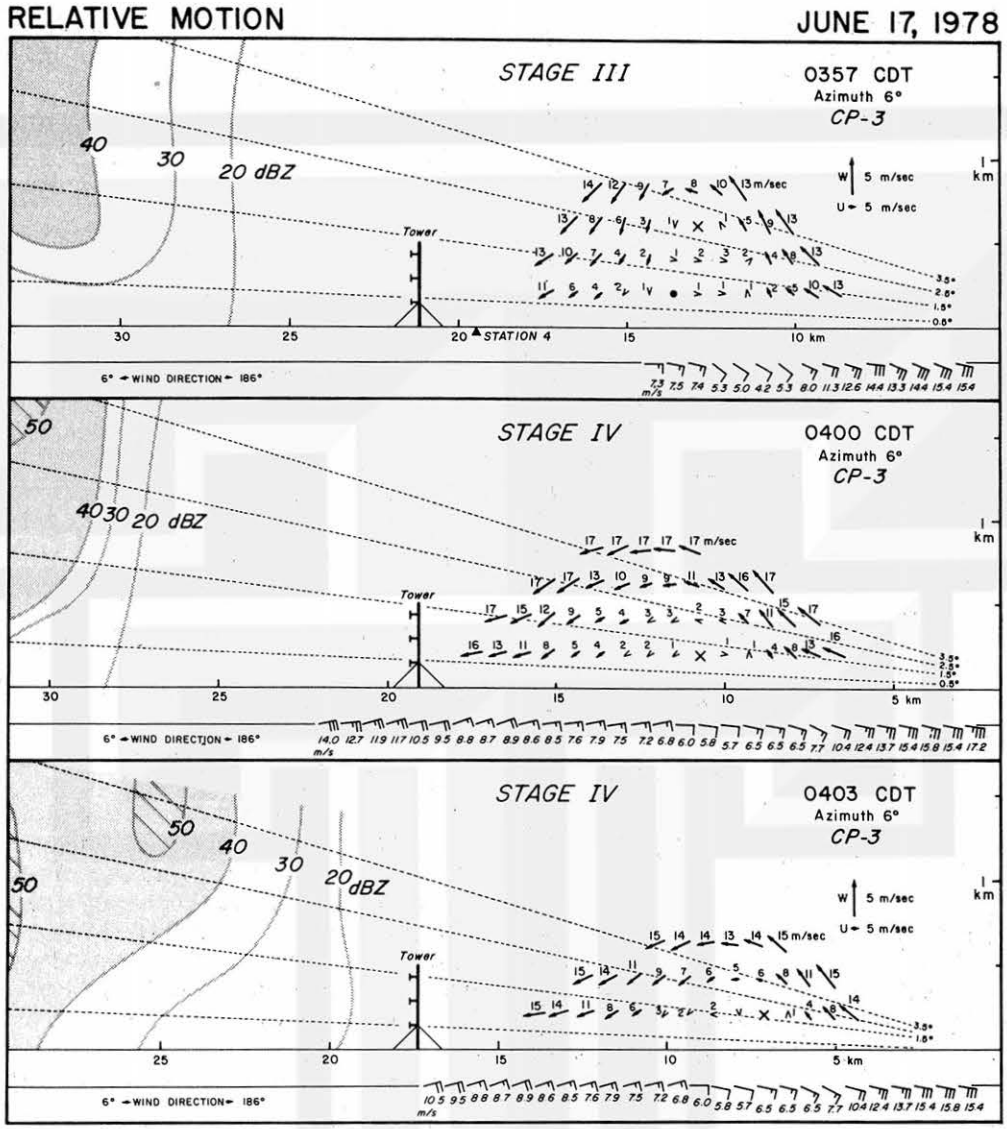

FIG. 21. RHI cross sections of the gust front-relative motion for Case B from YKV at 0357 (stage III), 0400 (stage IV), and 0403 (stabe IV) CDT. The "X" denotes the relative circulation center. The speeds of the Doppler wind vectors are labeled in the figure.

a simplified model will be derived. It is assumed that the flow is frictionless, irrotational, homogeneous and is confined to the x–z plane perpendicular to the gust front. The equation of motion in the x direction reduces to,

$$\frac{\partial u}{\partial t} + u\frac{\partial u}{\partial x} = -\frac{1}{\rho}\frac{\partial p}{\partial x} = \text{const} = C. \qquad (12)$$

Using the time–space conversion, a derivative in space can be converted into a derivative in time. Thus Eq. (12) becomes

$$\frac{\partial u}{\partial t} + \frac{u}{V}\frac{\partial u}{\partial t} = C, \qquad (13)$$

where V = the propagation speed of the gust front. Eq. (13) can be rewritten as

$$\frac{\partial}{\partial t}\left(u + \frac{u^2}{2V}\right) = C \qquad (14)$$

or

$$(u^2 + 2Vu)_t = 2VC\Delta t, \qquad (15)$$

where the equation has been integrated from $t = 0$ to $t = t$, and u is assumed to be zero at the initial time.

Eq. (15) is a simple quadratic in u and can be easily solved. The results are shown in Table 5.

There is good agreement between the observed and calculated decrease of wind speed in the warm air, despite the simplicity of the model. Apparently, the gradient of the nonhydrostatic pressure in the direc-

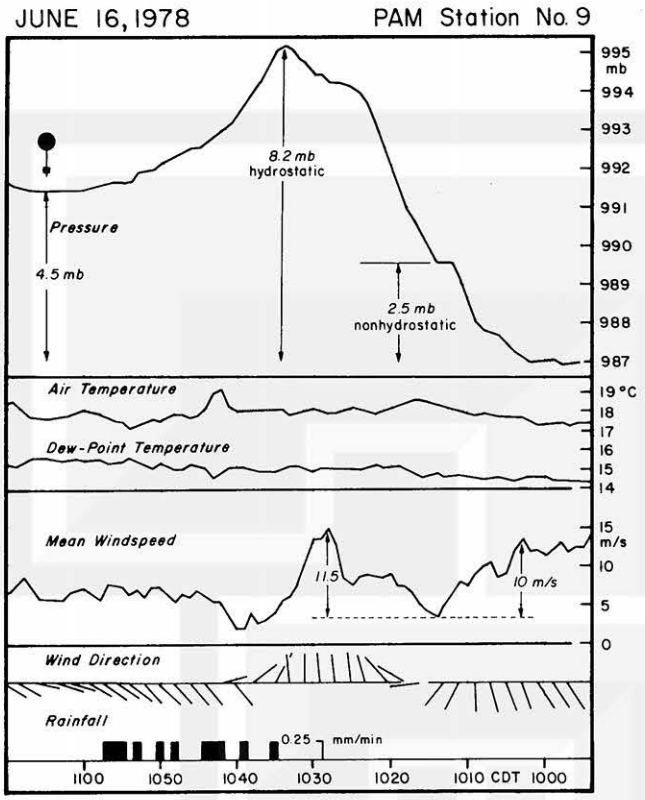

FIG. 22. Surface observations at YKV during the passage of Case A. The gust front was in stage III of its life cycle. Launch time of the rawinsonde is indicated above the pressure trace.

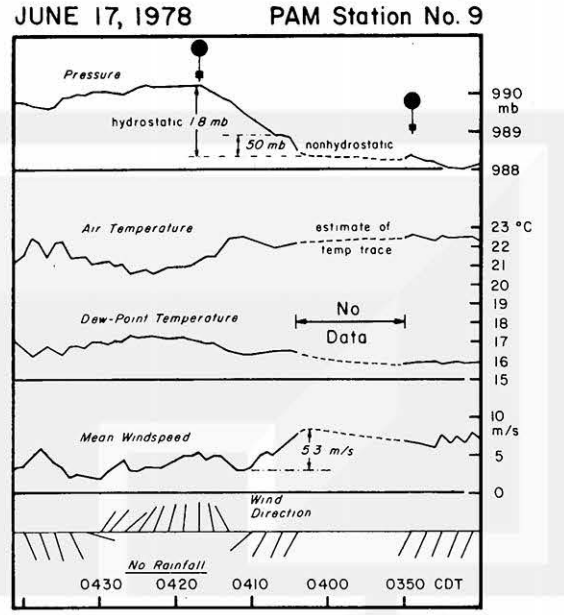

FIG. 24. Surface observations at YKV during the passage of Case B. The gust front was in stage IV of its life cycle. Launch times of the rawinsonde are indicated above the pressure trace.

tion perpendicular to the frontal interface is responsible for the decrease in the normal component of the wind speed to a minimum before the arrival of the cold air. This wind speed minimum may be regarded as "the calm before the storm" described by numerous observers and perhaps most dramatically shown in Fig. 22.

A final observation in Figs. 22 and 24 needs to be mentioned. At the same time as the wind direction shifts, the pressure levels off to a constant level. This signifies the maximum value of the nonhydrostatic pressure at the gust front. The hydrostatic pressure due to the arrival of the cold air is responsible for the total pressure rise following the nonhydrostatic pressure.

c. *"Dry pocket" in the upper levels of the outflow*

After examining the rawinsonde data for Case C, a curious feature was noted in the humidity data. A dry layer appears at the top of the cold air (Fig. 27).

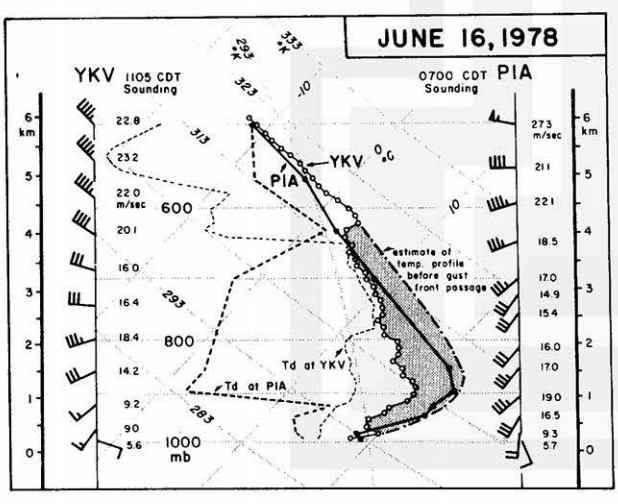

FIG. 23. Rawinsonde data from YKV at 1105 CDT and PIA at 0700 CDT (1200 GMT). The dashed-dot line is the estimate of the temperature profile before the passage of Case A.

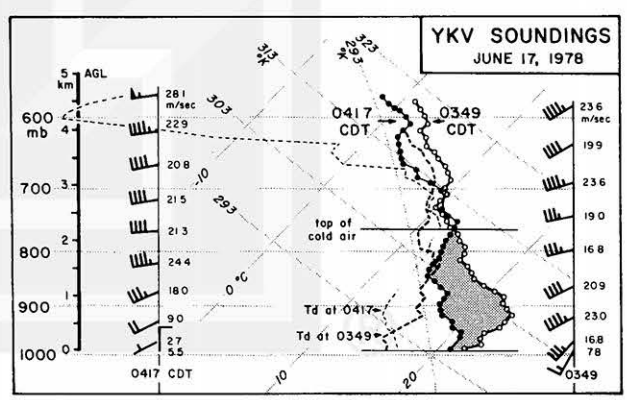

FIG. 25. Rawinsonde data from launchings at 0349 and 0417 CDT at YKV for Case B.

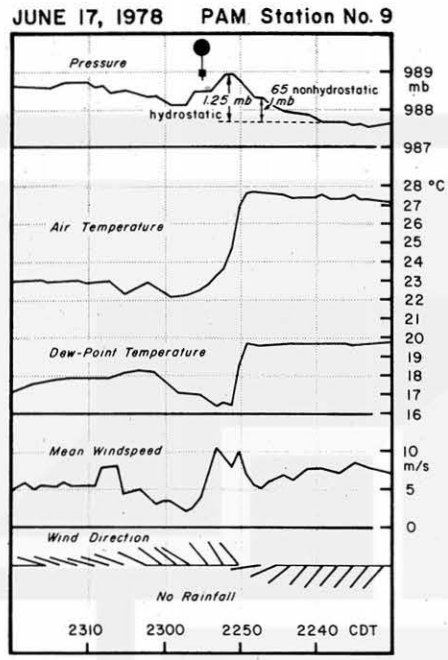

FIG. 26. Surface observations at YKV during the passage of Case C. The gust front was in stage III of its life cycle. The launch time of the rawinsonde is shown above the pressure trace.

Analysis of the vertical structure of the wet-bulb potential temperature for Case C (not shown) revealed that this layer had the same thermodynamic characteristics as the outflow air near the surface. Apparently, the sounding penetrated the low-level outflow air that was lifted vertically at the frontal boundary and advected back by the circulation within the head. This is shown schematically in Fig. 28.

d. Model of the gust front based on surface observations

Based on all of the surface observations during NIMROD, a model of the gust front in stages II and III is presented in Fig. 29. Since the surface observations are a function of the stability of the atmosphere, the model in Fig. 29 is based on a neutral atmosphere. Table 6 is the sequence of meteorological events during the passage of the gust fronts as a function of the elapsed time after the initial pressure rise. These results are consistent with those of numerous researchers.

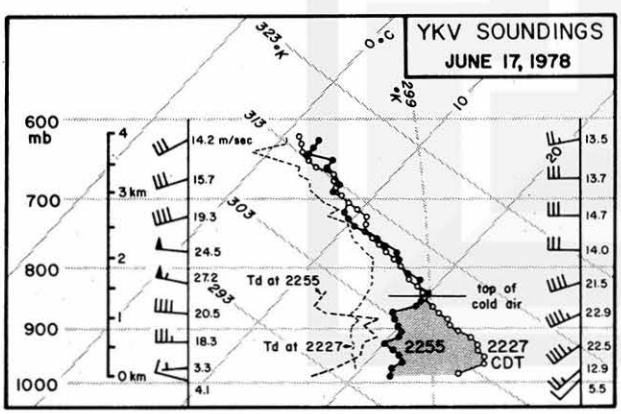

FIG. 27. Rawinsonde launchings for 2227 and 2255 CDT at YKV for Case C.

TABLE 3. Calculations of the hydrostatic pressure behind the gust front.

	Case A	Case B	Case C
$\bar{T}_{warm}$ (°C)	16.19	19.20	24.76
$\bar{T}_{cold}$ (°C)	13.00	16.15	20.76
Cold air depth (m)	3953	2236	1340
Calculated hydrostatic pressure rise (mb)	5.2	1.6	1.2
Observed hydrostatic pressure rise (mb)	4.5	1.8	1.3

6. Propagation speed of the gust front

Goff (1975, 1976) proposed that Eq. (16) would govern the propagation speed of the gust front, where U is the maximum speed observed normal to the front in the cold air:

$$V = 0.67U. \tag{16}$$

The effects of the warm ambient air were ignored since it was typically lifted over the cold air outflow. The depth of the cold air was also ignored in his calculations. Speeds were derived using Eq. (16) for all of the gust fronts observed during NIMROD and none were found to agree with the observed values.

The density current model appears to consider all of the thermodynamic conditions necessary to accurately describe the motion of the gust front. The equation for the speed of the leading edge of a density

TABLE 4. Nonhydrostatic pressure calculations.

	Case A	Case B	Case C
ρ_c (density of cold air) $\times 10^{-3}$ (g cm^{-3})	1.189	1.171	1.165
ρ_w (density of warm air) $\times 10^{-3}$ (g cm^{-3})	1.183	1.163	—
V_c (windspeed in the cold air) (m s^{-1})	15.0	5.0	10.0
V_w (windspeed in the warm air) (m s^{-1})	13.0	7.5	—
P_{nhc} (nonhydrostatic pressure in the cold air) (mb)	1.34	0.15	0.58
P_{nhw} (nonhydrostatic pressure in the warm air) (mb)	1.00	0.33	—
P_t (total nonhydrostatic pressure) (mb)	2.34	0.48	0.58
P_o (observed nonhydrostatic pressure increase) (mb)	2.50	0.50	0.65

TABLE 5. The effect of the gradient of nonhydrostatic pressure on the windspeed in the warm air.

	Case A	Case B
C (cm s^{-2})	1.47	1.14
V (m s^{-1})	20.0	5.5
Δt (min)	12	7
Δu_c (calculated decrease in windspeed) (m s^{-1})	8.7	3.6
Δu_o (observed decrease in windspeed) (m s^{-1})	10.0	5.3

current is

$$V = k\left(gd\,\frac{\bar{\rho}_c - \bar{\rho}_w}{\bar{\rho}_w}\right)^{1/2}. \qquad (17)$$

where g = gravitational acceleration, d = depth of the outflow, $\bar{\rho}_c$ = mean density in the cold air, $\bar{\rho}_w$ = mean density in the warm air and k = internal Froude number (ratio of the inertial force to the force of gravity).

Using the rawinsonde data, mean vertical densities in the warm and cold air were calculated. By substituting the observed propagation speed into Eq. (17), values of k could be compared with those found in the literature to establish if the gust front was dynamically similar to a density current. In Table 7 a mean value of k was calculated to be 0.77.

To compensate for the late balloon launching of Case A, a mean temperature in the cold air was calculated that would account for an 8.2 mb rise in the hydrostatic pressure (Fig. 22). A new temperature sounding was derived by subtracting 1.8°C from the old sounding. Assuming that the depth of the cold air did not change, a new mean density was derived. This temperature constant seems reasonable since the cold air had been modifying for ~0.5 h.

When Eq. (17) was initially derived by von Kármán (1940), the value of k was 1.414 in a frictionless flow model. In subsequent lab models by Keulegan (1958), k was found to have an average value of 1.1 when the Reynolds number was greater than 1000. Both of these values of k are valid when d is the mean depth of the cold air. If the height of the head was used, the value of k is 0.78.

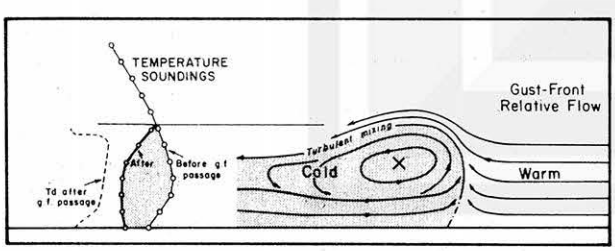

FIG. 28. Model of the thermodynamic structure of the gust front of Case C. Soundings before and after the gust front passage are shown.

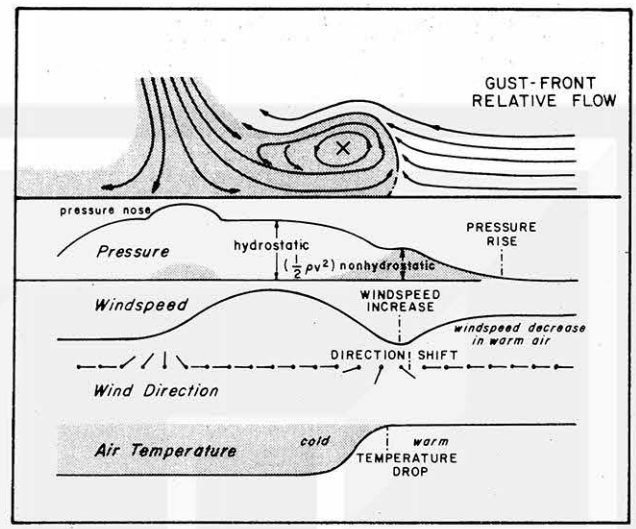

FIG. 29. Conceptual model of the surface observations during the passage of a gust front in stages II and III.

In Table 7, the depth of the cold air, as determined by the rawinsonde soundings during NIMROD, is assumed to be that of the head. Values of k obtained from the literature are shown in Table 8. Most researchers agree on a k value of ~0.75. Charba's large k value of 1.08 is a result of extrapolating the temperature profile above the tower level, leading to errors in the estimation of both the mean densities and height of the gust front head.

From the results of Table 7 and 8, it is concluded that the predominant driving force for the gust front is the horizontal pressure gradient acting across the interface caused by the greater hydrostatic pressure in the cold air. It is interesting to note that the vertical transfer of momentum provided by the downdraft does not play a role in determining the propagation speed. Of course, in the early stages (I or II), Eq. (17) could not be expected to accurately predict the motion of the outflow.

7. Summary and concluding remarks

The gust front is the leading edge of a mesoscale pressure dome many tens of kilometers in length that evolves through four stages in its life cycle. Examples of this time-dependent solution have been shown in great detail. A new finding was the precipitation roll that appears in stages II and III as the gust front

TABLE 6. Sequence of meteorological events as a function of elapsed time (minutes) after the pressure rise.

	Case A	Case B	Case C
Wind direction shift	12.3	17.3	5.2
Wind surge	13.0	17.4	6.1
Temperature break	none	19.5	6.4

begins to advance ahead of the squall line. The roll is defined as a reflectivity pattern of precipitation, revolving in a horizontal roll at the leading edge of a gust front.

The dynamic and thermodynamic structure of the gust front was presented in Sections 5 and 6. Although there were no direct measurements of stages I and II, Doppler velocity and reflectivity data tend to support the idea that the flow is similar to a vertical jet of fluid striking a plane surface. Using surface weather observations and serial rawinsonde soundings, it was determined that the dynamics of the subsequent stages (III and IV) are similar. These results are summarized below.

The pressure rise behind the gust front is solely a function of the cold outflow. The collision of the cold air behind the gust front with the warmer ambient air creates a nonhydrostatic pressure rise ahead of the gust front. This pressure attains a maximum value at the frontal boundary, and decreases uniformly to zero away from the boundary. A dry, cool layer at the top of the outflow was a result of the low-level outflow from the squall line that was lifted vertically at the frontal boundary and advected back by the circulation within the head of the gust front.

The nonhydrostatic pressure gradient is the main contributing factor for the decrease in the wind speed component normal to the gust front in the warm air. The wind speed reaches a minimum value at the time of the wind direction shift and is followed by an increase in the wind speed as the cold air arrives.

The equation for the propagation speed of a density current accurately predicts the movement of the gust front. The high-level momentum has little effect on the speed of the gust front once it has propagated ahead of the squall line.

This has been a comprehensive study of the gust front with the use of Project NIMROD data. It was the goal of this research to advance the understanding of the outflow from thunderstorms. Even if this has been accomplished there are still some questions that future research may answer. For example, there is evidence (Wakimoto, 1981) that the wind shift in some gust fronts may be confined to low levels. At higher levels the wind direction may shift back to a value close to the ambient direction, even though it is still within the outflow. These and similar problems will receive more attention as Doppler radar is used in the future to study the sub-storm scale.

TABLE 7. Propagation speed of the gust front.

	Case A	Case B	Case C
$\bar{\rho}_c$ (10^{-4} g cm^{-3})	9.66	10.41	10.87
$\bar{\rho}_w$ (10^{-4} g cm^{-3})	9.55	10.39	10.69
d (m)	3954	2235	1332
Observed propagation speed (m s^{-1})	20	7	13
k	0.76	0.71	0.87
		$\bar{k}$ = 0.77	

TABLE 8. k-values for different fluid and atmospheric phenomena.

Benjamin (1968)	0.75	Density current
Charba (1974)	1.08	Gust front
Daly and Pracht (1968)	0.70	Numerical model of a density current
Farquharson (1937)	0.90	Haboob
Georgi (1936)	0.74	Pampero secco
Keulegan (1958)	0.78	Density current
Simpson (1969)	0.72	Sea breeze

Acknowledgments. The author wishes to express his gratitude to Professor T. Theodore Fujita for his guidance. The author also wishes to thank Professors R. R. Braham, Jr., H.-L. Kuo, W. H. Reid and R. C. Srivastava for their advice and suggestions. Fig. 1 of this paper was drafted by Prof. Fujita; all subsequent figures were drafted by the author. Meteorological results reported in this paper have been sponsored by NOAA under grants NA80AA-D-00001, by NASA NGR 14-001-008, and by NSF ATM 79-21260.

APPENDIX

Specifications of the Three Doppler Radars

	ORD NCAR† CP-4 radar	YKV NCAR CP-3 radar	CHL ISWS* radar
Frequency	5460 MHz	5500 MHz	2749 MHz
Wavelength	5.49 cm	5.45 cm	10.91 cm
Pulse repetition frequency	1250 s^{-1}	1250 s^{-1}	975 s^{-1}
Maximum unambiguous velocity	±17.2 m s^{-1}	±17.0 m s^{-1}	±26.6 m s^{-1}
Gate length	210 m	210 m	150 m

* Illinois State Water Survey.
† National Center for Atmospheric Research.

REFERENCES

Batton, L. J., 1959: *Radar Observations of the Atmosphere.* University of Chicago Press, 324 pp.

Benjamin, J. B., 1968: Gravity current and related phenomena. *J. Fluid Mech.*, **31,** 209–248.

Brown, H. A., 1960: Report on radar thin lines. *Proc. Eighth Weather Radar Conf.*, Boston, Amer. Meteor. Soc., 65–72.

Byers, H. R., and R. R. Braham, Jr., 1949: *The Thunderstorm.* U.S. Govt. Print. Off., 287 pp.

Charba, J., 1974: Application of the gravity current model to analysis of squall-line gust fronts. *Mon. Wea. Rev.*, **102,** 140–156.

Colmer, M. J., 1971: On the character of thunderstorm gust fronts. Royal Aircraft Establishment, Bedford, England, 11 pp.

Daly, B. J., and W. E. Pracht, 1968: Numerical study of density-current surges. *Phys. Fluids*, **10,** 15–30.

Farquharson, J. S., 1937: Haboobs and instability in Sudan. *Quart. J. Roy. Meteor. Soc.*, **63,** 393–414.

Fawbush, E. J., and R. C. Miller, 1954: A basis for forecasting peak wind gusts in non-frontal thunderstorms. *Bull. Amer. Meteor. Soc.*, **35,** 14–19.

Fujita, T. T., 1957: Three-dimensional mesoanalysis of a squall line. Res. Rep. No. 1, Contract DA-36-039-SC-64656, Illinois State Water Survey, 19 pp.

——, 1963: Analytical mesometeorology: A review. *Severe Local Storms, Meteor. Monogr.*, No. 27, Amer. Meteor. Soc., 77–125.

——, 1978: Manual of downburst identification. SMRP Res. Pap. No. 156, Dept. Geophys. Sci., University of Chicago, 104 pp.

Georgi, J., 1936: Pampero secco vom 17 Juli 1935. *Der Seewart*, **7,** 199–205.

Goff, R. C., 1975: Thunderstorm outflow kinematics and dynamics. NOAA Tech. Memo., ERL NSSL-75, National Severe Storms Laboratory, Norman, OK, 63 pp.

——, 1976: Vertical structure of thunderstorm outflows. *Mon. Wea. Rev.*, **104,** 1429–1440.

——, J. T. Lee and E. A. Brandes, 1977: Gust front analytical study. National Severe Storms Laboratory, 125 pp. [NTIS FAA-RD-77-119].

Goldman, J. L., and P. W. Sloss, 1969: Structure of the leading edge of thunderstorm cold air outflow. *Preprints Sixth Conf. on Severe Local Storms*, Chicago, Amer. Meteor. Soc., 75–79.

Greene, G. E., J. A. Karrell and P. A. Mandics, 1977: An analysis of the gust front hazard. *Preprints Tenth Conf. on Severe Local Storms*, Omaha, Amer. Meteor. Soc., 151–153.

Hall, F. F., W. D. Neff and T. V. Frazier, 1976: Wind shear observations in thunderstorm density currents. *Nature* **264,** 408–411.

Huschke, R. E., 1959: *Glossary of Meteorology.* Amer. Meteor. Soc., 638 pp.

Keulegan, G. H., 1958: The motion of saline fronts in still water. U.S. Natl. Bur. Stand., Rep. No. 5831, 28 pp.

Middleton, G. V., 1966: Experiments on density and turbidity currents, Part I: Motion of the head. *Can. J. Earth Sci.*, **3,** 523–546.

Mitchell, K. E., and J. B. Hovermale, 1977: A numerical investigation of the severe thunderstorm gust front. *Mon. Wea. Rev.*, **105,** 657–675.

Newton, C. W., 1963: Dynamics of severe convective storms. *Severe Local Storms, Meteor. Monogr.*, No. 27, Amer. Meteor. Soc., 33–55.

Simpson, J. E., 1969: A comparison between laboratory and atmospheric density currents. *Quart. J. Roy. Meteor. Soc.*, **95,** 758–765.

——, 1972: Effects of the lower boundary on the head of a gravity current. *J. Fluid Mech.*, **53,** 759–768.

——, D. A. Mansfield and J. R. Milford, 1977: Inland penetration of sea-breeze fronts. *Quart. J. Roy. Meteor. Soc.*, **103,** 47–76.

Tepper, M., 1950: A proposed mechanism of squall lines: the pressure jump line. *J. Meteor.*, **7,** 21–29.

von Kármán, T., 1940: The engineer grapples with nonlinear problems. *Bull. Amer. Math. Soc.*, **46,** 615–683.

Wakimoto, R. M., 1981: Investigations of thunderstorm gust fronts using Project NIMROD data. Ph.D. thesis, Dept. Geophys. Sci., University of Chicago, 129 pp.